

DTIC FILE COPY

①

AD-A230 356



DTIC  
ELECTE  
JAN 07, 1991  
S B D

A COMPARISON  
OF  
MOLECULAR VIBRATION MODELING  
FOR  
THERMAL NONEQUILIBRIUM AIRFLOW  
THESIS

Kenneth J. Moran, Captain, USAF

DEPARTMENT OF THE AIR FORCE  
AIR UNIVERSITY  
**AIR FORCE INSTITUTE OF TECHNOLOGY**

Wright-Patterson Air Force Base, Ohio

**DISTRIBUTION STATEMENT A**  
Approved for public release  
Distribution Unlimited

AFIT/GAE/ENY/90D-17

①

A COMPARISON  
OF  
MOLECULAR VIBRATION MODELING  
FOR  
THERMAL NONEQUILIBRIUM AIRFLOW

THESIS

Kenneth J. Moran, Captain, USAF

AFIT/GAE/ENY/90D-17

DTIC  
ELECTE  
JAN 07 1991  
S B D

Approved for Public release; distribution unlimited

AFIT/GAE/ENY/90D-17

A COMPARISON OF MOLECULAR VIBRATION MODELING  
FOR THERMAL NONEQUILIBRIUM AIRFLOW

THESIS

Presented to the Faculty of the School of Engineering  
of the Air Force Institute of Technology

Air University

In Partial Fulfillment of the  
Requirements for the Degree of  
Master of Science in Aeronautical Engineering

Kenneth J. Moran, B.S.

Captain, USAF

December 1990

Approved for Public release; distribution unlimited

## Acknowledgements

I dedicate this work to Wayne P. Wilsdon, a friend and fellow CFDer who was an inspiration to everyone that knew him.

I would like to thank my thesis advisor Capt Phil Beran. Our thoughtful discussions helped "smooth out those instabilities" many times.

Additionally, I appreciated the help and friendship of Capt Mark Driver. I often sought out Mark for ideas, and never came away empty. Thanks especially for helping me with the Copenhagen factor. It played a key role during those day-long computing sessions.

I would like to thank my sponsor Dr. Joseph Shang, from the Wright Engineering Development Center. Many discussions with Dr. Shang and his group provided helpful guidance. Also, I thank the Ohio Supercomputer Center for use of their computer facilities, without which this research would not have been possible.

Most importantly I thank my wife, Tracy. She was patient when I was late; she was forgiving when I was forgetful. Thanks for being so understanding during those long nights spent alone.

"Any theory is better than no theory at all." A.B.

Kenneth J. Moran

## Table of Contents

Preface . . . . .	ii
List of Figures . . . . .	v
List of Tables . . . . .	viii
List of Symbols . . . . .	ix
Abstract . . . . .	xiii
I. Introduction . . . . .	1
A. Historical Background . . . . .	2
Numerical Analysis of Blunt-Body Flows . . . . .	2
Development of TVD/Roe Schemes . . . . .	3
B. High-Temperature Effects . . . . .	6
C. Outline of Study . . . . .	8
D. Findings . . . . .	9
II. Mathematical Model . . . . .	10
A. Assumptions . . . . .	10
B. Governing Equations . . . . .	12
1-D Shock Tube . . . . .	12
Sphere . . . . .	14
C. The Roe-averaged State . . . . .	16
D. Initial and Boundary Conditions . . . . .	17
III. Vibrational Excitation Theory . . . . .	19
A. Equilibrium Vibrational Energy . . . . .	19
B. Nonequilibrium Relaxation . . . . .	22
Millikan and White Model . . . . .	22
Park Model . . . . .	23
IV. High-Temperature, Shock Tube Results . . . . .	25
A. Perfect Gas . . . . .	25
B. Vibrational Effects . . . . .	29
Density Ratio Calculations . . . . .	33
Relaxation Times . . . . .	37
Park Model Versus Millikan and White Model . . . . .	40
V. Blunt-Body Solutions for a Perfect Gas . . . . .	43
A. Solution Flow Structure . . . . .	43
B. Numerical Issues . . . . .	47
Sensitivity Near Symmetry Line . . . . .	47
Nonphysical Solutions . . . . .	50
Grid Sensitivity . . . . .	52

VI.	Equilibrium/Nonequilibrium Blunt-Body Solutions . . . . .	54
A.	Shock Standoff Distances . . . . .	54
B.	Relaxation in Stagnation Region . . . . .	60
C.	Molecular Vibration Model Tradeoffs . . . . .	64
VII.	Conclusions and Recommendations . . . . .	66
A.	Solution Sensitivity to Axisymmetric Equations of Motion . . . . .	67
B.	Accuracy Versus Computational Complexity . . . . .	67
C.	Recommendations for Follow-on Study . . . . .	69
Appendix A:	Derivations of Governing Equations . . . . .	70
Appendix B:	Derivation of Flux Jacobians, Eigenvalues, and Eigenvectors . . . . .	76
Bibliography	. . . . .	82
Vita	. . . . .	86

<b>Accession For</b>	
NTIS GRA&I	<input checked="checked" type="checkbox"/>
DTIC TAB	<input type="checkbox"/>
Unannounced	<input type="checkbox"/>
Justification	
By	
Distribution/	
Availability Codes	
Dist	Avail and/or Special
A-1	

## List of Figures

Figure 1	Theoretical Shock Standoff Distance . . .	7
Figure 2	Shock Tube Schematic . . . . .	13
Figure 3	Pressure Profiles for Perfect Gas Model Applied to Shock Tube . . . . .	25
Figure 4	Velocity Profiles for Perfect Gas Model Applied to Shock Tube . . . . .	26
Figure 5	Density Profiles for Perfect Gas Model Applied to Shock Tube . . . . .	26
Figure 6	Temperature Profiles for Perfect Gas Model Applied to Shock Tube . . . . .	27
Figure 7	Nonphysical Discontinuity in Shock Tube .	28
Figure 8	Pressure Profile Comparison for Shock Tube	29
Figure 9	Velocity Profile Comparison for Shock Tube	30
Figure 10	Density Profile Comparison for Shock Tube	30
Figure 11	Temperature Profile Comparison for Shock Tube . . . . .	31
Figure 12	Vibrational Relaxation in Shock Tube . .	32
Figure 13a	Experimental Density Interferogram (Shock Tube, $M=2$ ) . . . . .	34
Figure 13b	Nonequilibrium Density Interferogram (Shock Tube, $M=2$ ) . . . . .	34
Figure 13c	Equilibrium Density Interferogram (Shock Tube, $M=2$ ) . . . . .	34
Figure 14a	Experimental Density Interferogram (Shock Tube, $M=6$ ) . . . . .	35
Figure 14b	Nonequilibrium Density Interferogram (Shock Tube, $M=6$ ) . . . . .	35
Figure 14c	Equilibrium Density Interferogram (Shock Tube, $M=6$ ) . . . . .	35
Figure 15	Density Ratios Across a Moving Shock . .	37

Figure 16	Oxygen and Nitrogen Relaxation Times normalized to 1 atm. . . . .	38
Figure 17	Relaxation Times for Air, Normalized to 1 atm . . . . .	39
Figure 18	Comparison of Relaxation Times for Two Temperature Models. . . . .	41
Figure 19	Computed versus Experimental Shock Standoff Distance (Nonequilibrium Model). . . . .	44
Figure 20	Sonic Line Location for a Sphere at $M=7.0$ . . . . .	45
Figure 21	Sonic Line Location for a Cylinder at $M=7.0$ . . . . .	45
Figure 22	Experimental Pressure Coefficients Around the Forward Portion of Hemisphere Cylinder, $M=5.7$ . . . . .	46
Figure 23	Pressure Coefficients from Perfect Gas Calculations. . . . .	47
Figure 24	Mach Contours for a Sphere at $M=5.7$ . . .	48
Figure 25	Mach Contours for a Cylinder at $M=5.7$ . .	48
Figure 26	Surface Pressure Coefficients for a Cylinder at $M=5.7$ . . . . .	49
Figure 27	Nonphysical Recirculation Phenomenon in Stagnation Region . . . . .	51
Figure 28	Effect of Axial Node Spacing on Shock Standoff Distance . . . . .	53
Figure 29	Density Contours for a Sphere at $M=6.0$ .	55
Figure 30	Temperature Contours for a Sphere at $M=6.0$ . . . . .	56
Figure 31	Mach Contours for a Cylinder at $M=5.0$ . .	57
Figure 32	Mach Contours for a Cylinder at Mach 7.0.	58
Figure 33	Temperature Contours for a Sphere at $M=8.0$ , Using Present Nonequilibrium Model	60
Figure 34	Temperatures Along the Stagnation Line. .	62



Figure 35	Temperature Comparison within the Shock Layer (Oxygen -vs- Nitrogen) . . . . .	62
Figure 36	Surface Temperature Distributions for M=5.7. . . . .	63

## List of Tables

Table I	Calculations across a Moving Shock (M = 5.75) . . . . .	36
Table II	Relaxation Times for Two-Temperature Models . . . . .	40
Table III	Shock Standoff Distances for Hemisphere Cylinder at M=5.7 . . . . .	59
Table IV	CPU Requirements for each Vibrational Model . . . . .	65

### List of Symbols

Symbol	Definition
$A$	flux Jacobian for x direction
$B$	flux Jacobian for y direction
$c$	speed of sound
$\bar{c}$	average molecular speed
$c_p$	specific heat at constant pressure
$c_v$	specific heat at constant volume
$D$	density of Roe averaging
$\tilde{e}$	internal energy
$e$	internal energy per unit mass
$e_{vib}$	vibrational energy per unit mass
$E$	flux vector in x direction
$\tilde{E}$	flux vector in $\xi$ direction
$E_{total}$	total energy per unit volume
$E_{vib}$	vibrational energy per unit volume
$F$	flux vector in y direction
$\tilde{F}$	flux vector in $\eta$ direction
$H$	total enthalpy
$i$	$\xi$ index
$j$	$\eta$ index
$\tilde{J}$	Jacobian of the transformation
$k$	Boltzmann constant
$k_1, k_2, K_\xi$	constants based on metrics

$M_\infty$	freestream Mach number
$M_s$	molecular weight of species s
$\bar{n}$	number density of mixture
$p$	pressure
$Q_{vib}$	partition function for molecular vibration
$Q_{T-v}$	rate of energy transfer(Landau-Teller form)
$R$	eigenvector, Riemann invariant
$R$	radius of blunt-body
$R$	gas constant
$S$	source term
$t$	time
$t_c$	Park relaxation time
$T$	translational/rotational temperature
$T_{vib}$	vibrational temperature
$u$	x component of velocity
$U$	vector of dependent variables
$U_c$	contravariant velocity
$v$	y component of velocity
$W_v$	vibrational source term
$\gamma$	ratio of specific heats
$\delta_o, \Delta_o$	shock standoff distance
$\epsilon$	density ratio
$\kappa$	partial derivative of pressure w.r.t. $\tilde{e}$
$\mu_{sr}$	reduced mass of species s and r
$\eta$	transformed coordinate

$\theta, \Theta$	angular measure
$\theta_v$	characteristic vibrational temperature
$\xi$	transformed coordinate
$\rho$	density
$\sigma$	limiting cross-section
$\tau$	vibrational relaxation time
$\chi$	partial derivative of pressure w.r.t. $\rho$
$(\hat{\cdot})$	Roe-averaged quantity

#### Subscript Definition

$B$	body
$c$	contravariant
$i$	$\xi$ index
$j$	$\eta$ index
$MAX$	maximum value
$n$	normal, normal derivative
$o$	standoff
$r, s$	species
$Sh$	shock
$Stag$	stagnation quantity
$t$	total, tangential
$x$	differentiation with respect to $x$ direction
$y$	differentiation with respect to $y$ direction
$\eta$	differentiation with respect to $\eta$ direction

$\xi$                     differentiation with respect to  $\xi$  direction  
 $\infty$                    condition at infinity

#### Superscript Definition

$n$                     time level  
 $\alpha$                    0: two-dimensional, 1: axisymmetric  
 $*$                     dummy time index

Abstract

The effects of thermal nonequilibrium on flows about blunt bodies have not been studied numerically in isolation from chemical reactions. Typically, air is modeled as a perfect gas or as a chemically reacting mixture. In the former case, significant errors result at Mach numbers exceeding about 5. However, below Mach numbers around 8, the effects of chemical reactions are negligible. This study examines inviscid flow about a simple axisymmetric blunt-body at moderate hypersonic speeds (Mach numbers between 5-8). A first-order-accurate Roe scheme was used to compute solutions of the Euler equations assuming different gas models: perfect gas, thermal equilibrium, and thermal nonequilibrium. Two vibrational relaxation models were used to examine thermal nonequilibrium. Equilibrium and nonequilibrium shock standoff distances deviated 10-15 percent from perfect gas calculations. Nonequilibrium calculations produced striking temperature and density gradients in the stagnation region with an isolated "hot spot" near the shock.

A COMPARISON OF MOLECULAR VIBRATION MODELING  
FOR THERMAL NONEQUILIBRIUM AIRFLOW

I. Introduction

High velocities and Mach numbers, strong shock waves, high-temperature phenomena, and shock/boundary-layer interactions comprise a few aspects of hypersonic flows. Some of these features are viscous in nature, but others also occur in an inviscid environment. The inviscid blunt-body flow features a strong shock which is normal to the nose, a thin shock layer and thermo-chemical nonequilibrium. Viscous features include "entropy swallowing" by the boundary-layer, boundary-layer/shock interaction, and high heat-transfer rates. This study concerns the inviscid flow about blunt bodies in the absence of chemical reactions.

The very nature of high velocity and high-temperature fluid flow makes it difficult and expensive to analyze or test experimentally. Until recently, the mathematical nonlinearities associated with detached and curved shocks, as well as high-temperature gas interactions and reactions, have prevented a numerical approach to studying hypersonics. However, with advances in Computational Fluid Dynamics (CFD),



numerical solution techniques have become possible, and in fact preferable.

The neglect of high-temperature gas effects still limits the applicability of most numerical algorithms to hypersonic problems. To illustrate, consider a reentry vehicle traveling at 6 km/s. It will experience temperatures near the stagnation point of about 6,000 °K for a reacting gas, but would endure an astonishing (and unrealistically high) 15,000 °K in a calorically perfect gas (1:19). This simplistic example shows the importance of accurately modeling high-temperature flows.

In the rest of this chapter, the current status of both CFD and hypersonic aerodynamics will be highlighted, as they apply to this study.

#### A. Historical Background

##### Numerical Analysis of Blunt-Body Flows

The mixture of subsonic and supersonic regions in blunt-body flows make consistent analysis difficult to achieve. In fact, until 1966, no practical blunt-body solution existed to provide valid initial conditions for a method of characteristics solution in the supersonic region. This changed in 1966 when Moretti and Abbett published the first time-marching, finite-difference solution of the governing unsteady Euler equations. Since the unsteady Euler equations are hyperbolic in both subsonic and supersonic regions, they

are mathematically consistent. Although Moretti and Abbett employed the Lax-Wendroff finite-difference technique, the philosophy remained the same when MacCormack's explicit, predictor-corrector finite-difference method was later applied. MacCormack's method has been widely used throughout the 1970's and 1980's (1:169). Unfortunately, this method requires several points to capture shocks, imposes strict limits on time step size, and is not very robust. The restriction on time step size is particularly limiting, since it delays convergence and induces a factor of unpredictability into the solution process. A new class of schemes has recently arisen to address these issues, namely Total Variation Diminishing (TVD) schemes.

#### Development of TVD/Roe Schemes

Many different schemes and algorithms have evolved to solve the Euler equations (16,44,45,46). Most of these numerical schemes arose from examinations of the Riemann problem. The Riemann problem is governed by the 1-D inviscid and frozen flow equation:

$$\frac{\partial U}{\partial t} + \frac{\partial F}{\partial x} = 0 \quad (1)$$

$$@ \ t = 0 \quad U = \begin{cases} U_L & \text{if } x < 0 \\ U_R & \text{if } x > 0 \end{cases}$$

where  $U_L$  and  $U_R$  are the left and right interface states. By

replacing the initial data with an approximate distribution, which is constant and uniform over each discrete interval, we can solve the Riemann problem for each interval and get an "exact" solution to an "approximate" problem (36:344). This was first proposed by Godunov and is appropriately named Godunov's Method. As one might expect, this approach places the discontinuities at cell interfaces (35:358). Most of the upstream differencing schemes make use of the solution of the Riemann problem as a building block. These Riemann solvers divide the flux difference between neighboring states into component parts associated with each wave field (11) and has yielded great success in flow computation.

From a numerical point of view, however, it seems wasteful to solve exactly the Riemann problem at every interface. Therefore, some approximate solutions or solvers are preferred. This analysis uses Roe's method of "... exploiting the fact that the Riemann solution for any set of linear conservation laws is easily computed" (36:346). Here we replace  $F$  in Equation (1) with some linear function of  $U$  :

$$\frac{\partial U}{\partial t} + A \frac{\partial U}{\partial x} = 0 \quad (2)$$

where  $A$  is the Jacobian matrix  $\frac{\partial F}{\partial U}$ .

This approach is much more efficient. In addition to the complexity associated with solving the nonlinear Euler

equations, it is difficult to accurately resolve the shocks present at hypersonic speeds. For problems with strong shock waves or contact discontinuities, Total Variation Diminishing (TVD) schemes provide high-resolution, shock capturing without loss of smoothness. In other words, a shock is captured in only a few discrete nodes without sacrificing a smooth solution near the discontinuity. More formally, these TVD schemes comprise a class of conservative, nonoscillatory, shock capturing schemes (47:6). Additionally, when applied to a scalar, hyperbolic, conservation law, as (1) or (2), the total variation of a solution,  $TV(U)$ , given by:

$$TV(U) = \int_{-\infty}^{\infty} \left| \frac{\partial U}{\partial x} \right| dx \quad (3)$$

cannot increase with time (20:2). The first-order Roe scheme, which was used in this analysis, satisfies the TVD property for a scalar, hyperbolic equation.

Roe, who originally developed his algorithm in 1981, used information from two neighboring states to compute quantities at some intermediate state (35:357-372), much like simple straight averaging. Unlike straight averaging, however, Roe-averaging is mass weighted. Vinokur and Liu recently extended Roe's work for equilibrium and nonequilibrium flows (24,42). Chapter 2 provides some details about this averaging.

## B. High-Temperature Effects

Although many robust techniques use TVD schemes and approximate Riemann solvers, they still assume an ideal gas and neglect high-temperature effects such as molecular vibration, dissociation, and ionization. It is well known that high-temperature effects play an important role at hypersonic speeds. Particularly, the shock layer decreases in thickness as temperature behind the shock increases. This is caused by processes, other than the normal translational and rotational degrees of freedom in molecules, absorbing energy behind the shock. The first of these processes to develop, as temperature increases, is molecular vibration. When vibrational excitation absorbs energy, the temperature decreases. The decrease in temperature accompanies a rise in density, a decrease in  $\gamma$ , and ultimately results in a thinner shock layer (31:2). To illustrate, the following relation between density and shock standoff for an axisymmetric blunt-body is provided from Hayes and Probstein (12:160):

$$\Delta_o = \epsilon R_B \left[ 1 - \sqrt{\frac{8\epsilon}{3}} + \frac{8}{3}\epsilon + O(\epsilon^2) \right] \quad (4)$$

where  $\epsilon = \rho_1/\rho_2$ . Clearly, as  $\rho_2$  increases,  $\Delta_o$  decreases. Now by applying the hypersonic limit to the normal shock relation for density,  $\epsilon$  becomes:

$$\lim_{M \rightarrow \infty} \epsilon = \frac{\gamma-1}{\gamma+1}$$

This simple expression depends entirely on the value of  $\gamma$  within the shock-layer, and therefore the thermal state of the flow. The trend in shock standoff distance with decreasing  $\gamma$  can be seen in Figure 1.

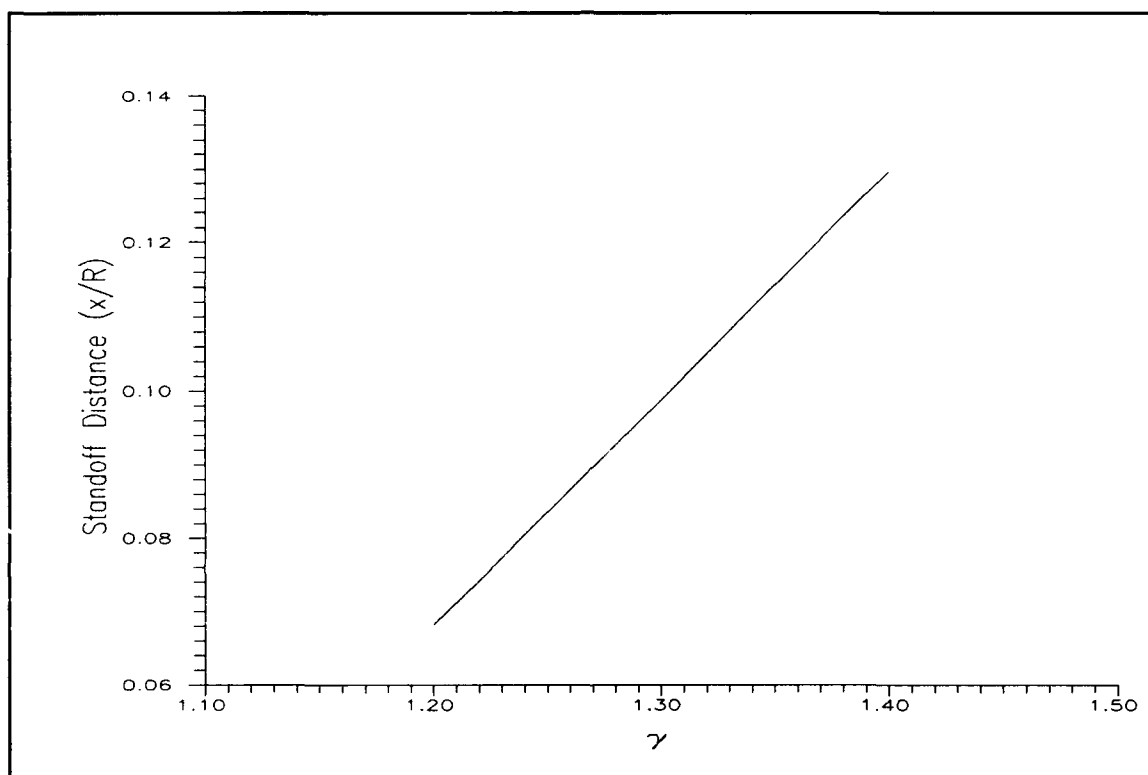


Figure 1      Theoretical Shock Standoff Distance

Much effort recently has been directed toward modeling thermal nonequilibrium phenomena. In fact, current schemes employ various vibration modeling techniques (5,9,27,31,39). However, this modeling is most often done in conjunction with chemical reactions. Since vibrational relaxation precedes dissociation, and the dissociation rate depends significantly

on the vibrational state, an accurate analysis of molecular vibration is required in isolation from the chemistry.

### C. Outline of Study

This study has three phases. In the first phase, the effects of high-temperature thermodynamic states (equilibrium/nonequilibrium) are investigated. Thermal equilibrium is analyzed by using variable heat capacities. The equilibrium analysis requires no change to, or expansion of, the equations of motion. The nonequilibrium analysis is accomplished by expanding the governing equations to include a vibrational energy equation. The rate of energy exchange between translational and vibrational energy modes will be examined using two different relaxation rate models. Chapter 3 details the theory associated with each model. Computed results are compared to experimental results for a shock tube.

During the second phase, a Roe scheme was modified for axisymmetric flow and a general coordinate system. The "Roe-averaged" state was derived by Roe for a perfect gas (35:357-372) and is outlined in Chapter 2. This phase established a perfect gas baseline for comparison throughout the study. Solutions are computed over the forward portion of a sphere for Mach numbers ranging from 5 to 8. Theoretical shock standoff distances, sonic line locations and pressure distributions are used to validate the algorithm.

For the third and final phase, contrasts of accuracy and computational complexity highlight the advantages of each model. This gives future investigators information about the tradeoffs associated with vibrational excitation modeling.

#### D. Findings

The first-order Roe scheme accurately predicted inviscid flow about a sphere. Additionally, large Courant numbers could be used during the analysis. Converged thermal nonequilibrium solutions were obtained in less than 1000 iterations.

Vibrational excitation caused shock standoff distances to decrease by about 10-20 percent. Subsequently, temperatures within the shock layer and on the body surface differed substantially from perfect gas calculations. Only the nonequilibrium analysis predicted a concentrated region of high temperatures near the shock.

Finally, this study revealed that using a thermal nonequilibrium model, with a Millikan and White relaxation rate, provided the best combination of accuracy and efficiency.



## II. Mathematical Model

Two different geometries were analyzed in this study, the 1-D shock tube and a simple axisymmetric blunt-body. First, the shock tube allowed comparisons between computed solutions and theory to ascertain the performance of the algorithm in one dimension and the accuracy of each molecular vibration model. Also, the relaxation phenomena could be analyzed without the complicating effects of grid transformations and geometry. The blunt-body problem provided a more comprehensive check on the accuracy in computing flows around more physically realistic geometries. As pointed out by Reference 21, "at hypersonic flight speeds all bodies must be blunt-nosed to some extent to reduce the heat transfer rate to manageable proportions."

### A. Assumptions

To fully isolate the kinetic behavior, the following assumptions were made throughout the investigation:

1. Inviscid, nonconducting flow
2. All energy modes decouple completely
3. No electronic effects
4. No dissociation or ionization

The decoupling of energy modes follows from an analysis of the Schrodinger equation. This equation is a time-dependent equation which governs two interacting particles. Translational energy decouples mathematically by a simple

separation of variables in the Schrodinger equation (15). Since the internucleic spacing closely matches the classical equilibrium spacing (15), a further decoupling of rotation and vibration results. A more detailed discussion of the quantum mechanics of diatomic molecules can be found in Reference 15.

Although viscous drag and heat transfer cannot be determined, a comparison of density and temperature within the shock layer can be made. Ultimately these quantities will influence the size of gradients within a boundary-layer.

Some further assumptions for equilibrium air were made:

1. Vibrational mode in equilibrium with translation and rotation, but not necessarily fully excited.
2. The flow can be described by a single density and temperature.
3. A harmonic oscillator approximation for the molecular potential energy.
4. A characteristic vibrational temperature,  $\theta_v$ , of 3154.8 °K.

The term "fully excited" means that the specific internal energy increases linearly with  $T$  (41:133). This concept is used by anyone assuming a calorically perfect gas. A single density and temperature assumption simplifies the governing equations, and reduces the rank of the system to 4. Moreover a single harmonic oscillator can be used in the vibrational excitation analysis. A harmonic oscillator potential is a classical linear spring potential where the spring constant relates to the vibrational frequencies. In practice, these frequencies are determined from spectroscopic measurements.

Harmonic vibration reasonably predicts the vibrational energy states associated with quantum mechanics (15). Again the reader is referred to Reference 15 for a more thorough discussion of quantum and statistical mechanics.

No characteristic vibrational temperature explicitly exists for air. Therefore, those associated with oxygen and nitrogen were used to derive a mole-based  $\theta_{v_{air}}$ . These two constituents were selected since they comprise the primary diatomic species in air.

A harmonic oscillator potential, and the same characteristic vibrational temperature, were also used in the nonequilibrium analysis. Here, however, a different equation governs the energy associated with molecular vibration. This equation is provided in the next section.

## B. Governing Equations

### 1-D Shock Tube

The flow in an ideal shock tube is caused by the instantaneous rupture of a dividing wall, or diaphragm, that separates two fluids with different static pressures. A schematic of the flow field is as follows:

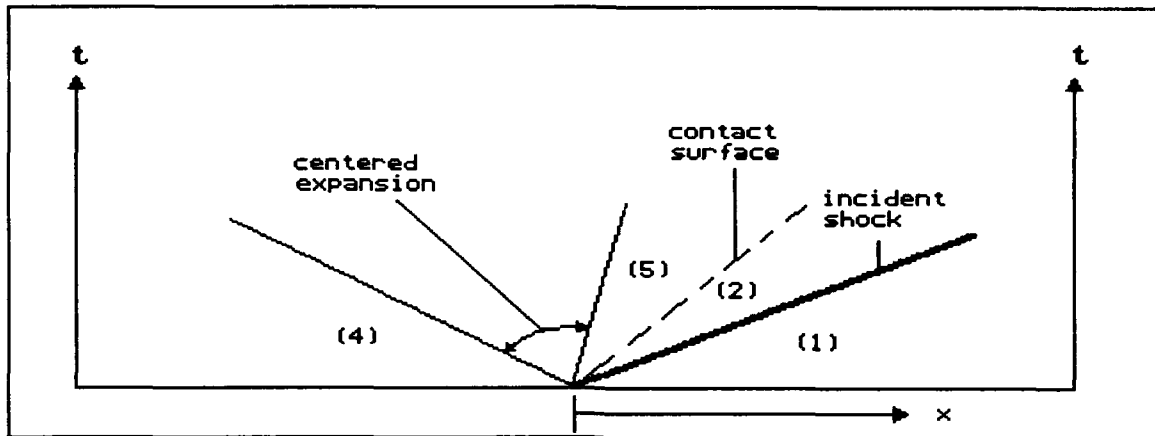


Figure 2 Shock Tube Schematic

For this analysis, the region between the shock wave and contact surface provide the proper physical environment for nonequilibrium study. Additionally, the shock tube is a Riemann problem which has an exact solution. The normal shock relations combine with Riemann invariants to produce the following expression involving the pressure jump across the shock:

$$\frac{p_4}{p_1} = \frac{p_2}{p_1} \left( 1 - \frac{(\gamma_4 - 1) (a_1/a_4) \beta}{(4\gamma_1^2 + 2\gamma_1(\gamma_1 + 1) \beta)^{1/2}} \right)^{-2\gamma_4/(\gamma_4 - 1)} \quad (5)$$

where,  $\beta \equiv \frac{p_2}{p_1} - 1$ ,  $a_1$  represents the speed of sound in front of the moving shock, and  $a_4$  the speed of sound in front of the expansion fan. The remainder of the exact solution is outlined in Reference 8.

For the shock tube, the continuity, momentum, and energy equations can be written in conservation form as:

$$\frac{\partial U}{\partial t} + \frac{\partial F}{\partial x} = 0 \quad (6)$$

where

$$U = \begin{bmatrix} \rho \\ \rho u \\ E_{total} \end{bmatrix} \quad F = \begin{bmatrix} \rho u \\ P + \rho u^2 \\ (P + E_{total})u \end{bmatrix}$$

### Sphere

The equations of motion for inviscid, non-conducting, axisymmetric flow can be written in conservation form as:

$$\frac{\partial U}{\partial t} + \frac{\partial F}{\partial x} + \frac{\partial G}{\partial y} = S \quad (7)$$

where

$$U = \begin{bmatrix} \rho y \\ \rho uy \\ \rho vy \\ E_{total}y \end{bmatrix} \quad F = \begin{bmatrix} \rho uy \\ (P + \rho u^2)y \\ \rho uvy \\ (P + E_{total})uy \end{bmatrix}$$

$$S = \begin{bmatrix} 0 \\ 0 \\ P \\ 0 \end{bmatrix} \quad G = \begin{bmatrix} \rho vy \\ \rho uvy \\ (P + v^2)y \\ (P + E_{total})vy \end{bmatrix}$$

Appendix A transforms and develops these equations for a general coordinate system in the manner described in Reference 38. When discretized, the equations of motion are evaluated

at cell centers. Additionally, at cell interfaces, the metrics were averaged using a finite volume approach (46:4).

Equilibrium analysis does not require any modification of the equations of motion. For the nonequilibrium analysis, however, the equations of motion must be expanded to include a separate equation for the vibrational energy of each species. Now  $U$  in Equation (5) becomes:

$$U = \begin{bmatrix} \rho_1 Y \\ \rho_2 Y \\ \rho u Y \\ \rho v Y \\ E_{total} Y \\ E_{vib_1} Y \\ E_{vib_2} Y \end{bmatrix} \quad (8)$$

The vibrational energy equation written in conservation form is (5:2).

$$\frac{\partial [E_{vib} Y]}{\partial t} + \frac{\partial [u E_{vib} Y]}{\partial x} + \frac{\partial [v E_{vib} Y]}{\partial y} = (Q_{T-v}) Y \quad (9)$$

where,

$$Q_{T-v} = \frac{\rho [e_{vib}|_T - e_{vib}|_{r_{vib}}]}{\tau}$$

$Q_{T-v}$  is the Landau-Teller form for the rate of energy exchange between translational and vibrational energy modes, and  $\tau$  is the relaxation time (19). The Landau-Teller rate equation assumes that the vibrational relaxation rate varies linearly with the difference in vibrational energies (32:235). This is the most widely used form for vibrational relaxation modeling

(4,5,9,16,27,33,40,43). Two different relaxation rate models were used to predict  $\tau$ . Chapter 3 describes the theory behind each model.

The linearized flux Jacobians used in the equilibrium and nonequilibrium analysis were obtained with Mathematica, which is a system for doing symbolic, algebraic and graphic mathematical computations. Appendix B contains a summary of the procedure and resulting eigenvalues and eigenvectors.

### C. The Roe-averaged State

When evaluating the dissipation term, some form of averaging is required at cell interfaces. The present scheme uses the "Roe-average". This Roe-averaged state was derived by Roe for a perfect gas, and generalized for both equilibrium and nonequilibrium flow by Vinokur (24,35,42). The reader is referred to these references for a complete derivation of the averaging. To summarize, Roe-averaging consists of,  $\hat{A}_{i+1/2} = \hat{A}(\hat{U}_{i+1/2})$  and  $\hat{U}_{i+1/2} = \hat{U}(U_i, U_{i+1})$ , and makes use of the ratio  $\rho_{i+1}/\rho_i$  such that:

$$\hat{U}_{i+1/2} = \frac{\rho_i^{1/2} u_i + \rho_{i+1}^{1/2} u_{i+1}}{\rho_i^{1/2} + \rho_{i+1}^{1/2}} = \frac{Du_i + u_{i+1}}{D + 1} \quad (10)$$

where,  $D = (\rho_{i+1}/\rho_i)^{1/2}$ . Since pressure is directly related to enthalpy for a calorically perfect gas, typically only velocity, enthalpy and the speed of sound need to be averaged. However, for the equilibrium and nonequilibrium analysis

pressure no longer directly relates to enthalpy and the partial derivatives of pressure, defined here as  $\kappa$  and  $\chi$ , also need to be averaged. A detailed discussion of these two parameters can be found in the next chapter, but the averaging for these quantities is quite involved and will not be included into this document. References 24,42 amply cover the derivations in full detail.

#### D. Initial and Boundary Conditions

The shock tube problem only requires that the initial solution have a high pressure side and low pressure side. It does not require any boundary conditions unless reflected shocks and waves are studied.

For the blunt-body problem, an initial condition was derived from an empirical shock location and shape, oblique shock relations, modified Newtonian theory, the equation of state and a constant enthalpy condition (1:190). The shock standoff distance and shock shape can be very closely approximated by the method in Reference 2. Oblique shock relations then determine values at the shock. Along the body, the initial condition assumes a Newtonian pressure distribution and linear velocity distribution. Throughout the field, velocities and pressures are interpolated between the body and shock. Finally, the adiabatic, constant enthalpy relation and equation of state determine temperature and density, respectively.



Boundary conditions which were simple, but would not degrade the accuracy of the solution were chosen for this study. For inviscid flow, tangency of velocity needs to be satisfied at the body surface. Reflection on density and total energy complete the surface boundary condition. Next, a supersonic inflow condition, and "no-change" outflow condition were imposed. Finally, at the symmetry line  $v$  and  $\frac{\partial v}{\partial r} \rightarrow 0$ . Several other boundary conditions were tried while trying to improve the solution:

BODY

1. Tangency and  
Normal Momentum (34:14)

SYMMETRY LINE

1. Zeroing the fluxes
2. Limiting form of the  
Equations of Motion(39:4)

Chapter 4 summarizes results from the different conditions.

### III. Vibrational Excitation Theory

Vibrational excitation can be modeled in three ways. We can ignore it, as with the perfect gas assumptions. We can also place it in equilibrium with the other energy modes, or we can treat it as a process that occurs at a finite rate. As described by Lambert (18:13):

In a sudden compression the whole energy goes initially to increase  $T_{tr}$ , and this is followed by relaxation to T-R and T-V energy transfer until equilibrium between the three modes is re-established. Such rapid compressions are produced by ultrasonic sound or by the passage of shock-fronts.

#### A. Equilibrium Vibrational Energy

The equilibrium model is based solely on statistical and quantum mechanics, which predicts that a partition function can be related to specific internal energy by the relation (41:128):

$$e_{vib} = RT^2 \frac{\partial(\ln Q_{vib})}{\partial T} \quad (11)$$

where  $Q_{vib}$  is the Partition Function, and

$$Q_{vib} = \frac{1}{1 - \exp(-\theta_v/T)}$$

Recall that  $\theta_v$  is the characteristic vibrational temperature and is constant. Additionally, since internal energy defines

temperature, the above relation for the vibrational energy, combined with the relations for fully excited translational and rotational energy, provide enough information to compute temperature.

$$\begin{aligned} e_{trans} &= \frac{3}{2}RT \\ e_{rot} &= RT \end{aligned} \tag{12}$$

Only for temperatures which exceed those where dissociation begins will the vibrational energy mode reach a fully-excited state.

As pointed out earlier, the equilibrium model required no expansion or modification of the governing equations. The increase in complexity finds its way into the problem through the linearization of the flux terms. For these terms, the partial derivatives of pressure, with respect to energy and density, were rederived. Utilizing the chain rule:

$$\kappa \equiv \left. \frac{\partial p}{\partial \tilde{e}} \right|_p = \left( \left. \frac{\partial p}{\partial T} \right|_p \right) \left( \left. \frac{\partial T}{\partial \tilde{e}} \right|_p \right) = \rho R \left. \frac{\partial T}{\partial \tilde{e}} \right|_p \tag{13}$$

where  $\tilde{e} = \rho e$ . Now from (11-12),

$$e = \frac{5}{2}RT + \frac{\theta_v R}{\exp(\theta_v/T) - 1} \tag{14}$$

$$\left. \frac{\partial T}{\partial \tilde{\epsilon}} \right|_p = \frac{1}{\frac{5}{2} \rho R + \frac{\exp(\theta_v/T) \left( \frac{\theta_v}{T} \right)^2 \rho R}{(\exp \theta_v/T - 1)^2}} \quad (15)$$

$$\kappa = \frac{1}{\frac{5}{2} + \frac{\exp(\theta_v/T) \left( \frac{\theta_v}{T} \right)^2}{(\exp \theta_v/T - 1)^2}} \quad (16)$$

Using the definition of pressure from Reference 42, leads to a convenient form for the second partial derivative of pressure:

$$P = \chi \rho + \kappa \tilde{\epsilon}$$

$$\text{where } \chi \equiv \left. \frac{\partial p}{\partial \rho} \right|_{\tilde{\epsilon}}.$$

Therefore,

$$\chi = RT - \frac{\kappa \tilde{\epsilon}}{\rho} \quad (17)$$

It is very interesting to note that (16) reduces to  $\kappa = \frac{2}{5}$  or  $(\gamma-1)$  for low temperatures. Then with  $\tilde{\epsilon} = \rho C_v T$  and  $\kappa = \gamma-1$ ,  $\chi$  from (17) vanishes. These are exactly the perfect gas relations where  $p = (\gamma-1)\rho e$ .

## B. Nonequilibrium Relaxation

Equilibrium for translation is attained in only a few collisions since there is free interchange of translational energy at every collision. Likewise, for temperatures in excess of a few hundred degrees, rotational equilibrium is attained in less than ten collisions (18:25). Molecular vibration, however, requires significantly more collisions and time to reattain equilibrium. The present nonequilibrium analysis accounts for this energy relaxation with a two-temperature model (30:488). One temperature,  $T$ , specifies the translational/rotational energy, and the other temperature,  $T_{vib}$ , defines the nonequilibrated vibrational energy. This analysis used the Landau-Teller form for the energy exchange between modes (19:34). This appears as a source term in the vibrational energy equation (see Chapter 2), and is a function of the relaxation time,  $\tau$ . To approximate the relaxation time, both the Millikan and White model and the Park model were tested. These models are both empirical, since a theoretical model has not been developed to date.

### Millikan and White Model

Millikan and White developed an empirical model to compute relaxation times for diatomic molecules(28:1). They found that  $\ln(\tau p)$  is linearly related to  $T^{-1/3}$  through the

following relation:

$$\tau_{sr} = \frac{1}{P_s} \exp [A_{sr} (T^{-1/3} - \mu_{sr}^{1/4}) - 18.42] \quad (18)$$

where,

$$A_{sr} = 1.16 \times 10^{-3} \mu_{sr}^{1/2} \theta_{v_s}^{4/3}$$

$$\mu_{sr} = \frac{M_s M_r}{(M_s + M_r)}$$

Here  $\tau_{sr}$  is the relaxation time for molecule s colliding with species r, and  $p_s$  is the partial pressure of the colliding particles (in atm). As Mach number increases, both  $p$  and  $T$  within the shock layer increase. This forces relaxation times to decrease.

#### Park Model

Park developed another model to improve relaxation rates at very high temperatures (31:4). The rate of change of vibrational energy in the molecule s, by collisions with species r, is given by:

$$Q_{(T-v)_s} = \frac{\rho [e_{vib_s}|_T - e_{vib_s}|_{T_{vib}}]}{\tau_{sr} + t_c} \left[ \frac{T_{sh} - T_{vib}}{T_{sh} - T_{vib_{sh}}} \right]^{S-1} \quad (19)$$

where

$$t_c = \frac{1}{c \sigma \bar{n}} \quad S = 3.5 \exp \left[ \frac{-T_{sh}}{5000} \right]$$

$$c = \left( \frac{8 k T}{\pi \bar{\mu}} \right) \quad \sigma = 1 \times 10^{-17} \left[ \frac{50,000}{T} \right]^2$$

The number density of the mixture is  $\bar{n}$ .  $k$  is the Boltzmann constant;  $\bar{\mu}$  defines the average mass and  $T_{sh}$  denotes the temperature behind the shock.  $c$  is the average molecular speed and  $\sigma$  is the limiting cross-section. Park modified the classical Landau-Teller model to account for the collision time,  $t_c$ . Unfortunately, he did not document the development of the last term, other than to state that it brought "calculated values into closer agreement with experimentally-determined values" (31:4). The vibrational energy,  $e_{vib}$ , is still determined using a harmonic oscillator for the partition function. The dependence, however, is now on the nonequilibrated, vibrational temperature,  $T_{vib}$  :

$$e_{vib_s} = \frac{R \theta_{v_s}}{\exp(\theta_{v_s}/T_{vib}) - 1} \quad (20)$$

Although this model yielded results closer to experimental values in Reference 31, no information on its application at moderate Mach numbers could be found.

#### IV. High-Temperature, Shock Tube Results

##### A. Perfect Gas

The upwind scheme with Roe averaging was very robust and produced qualitatively accurate solutions. Figures 3-6 demonstrate the accuracy of the algorithm developed. Here the distributions for density, pressure, velocity, and temperature, are plotted against the exact, theoretical solution.

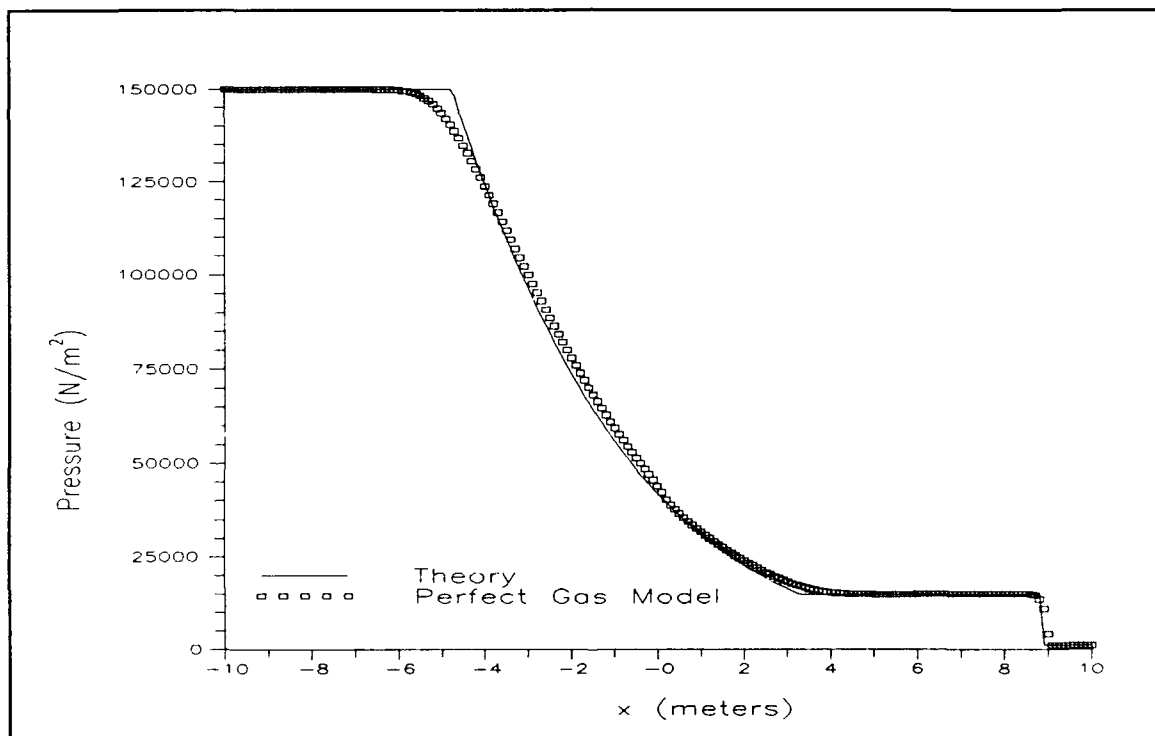


Figure 3      Pressure Profiles for Perfect Gas Model Applied to Shock Tube



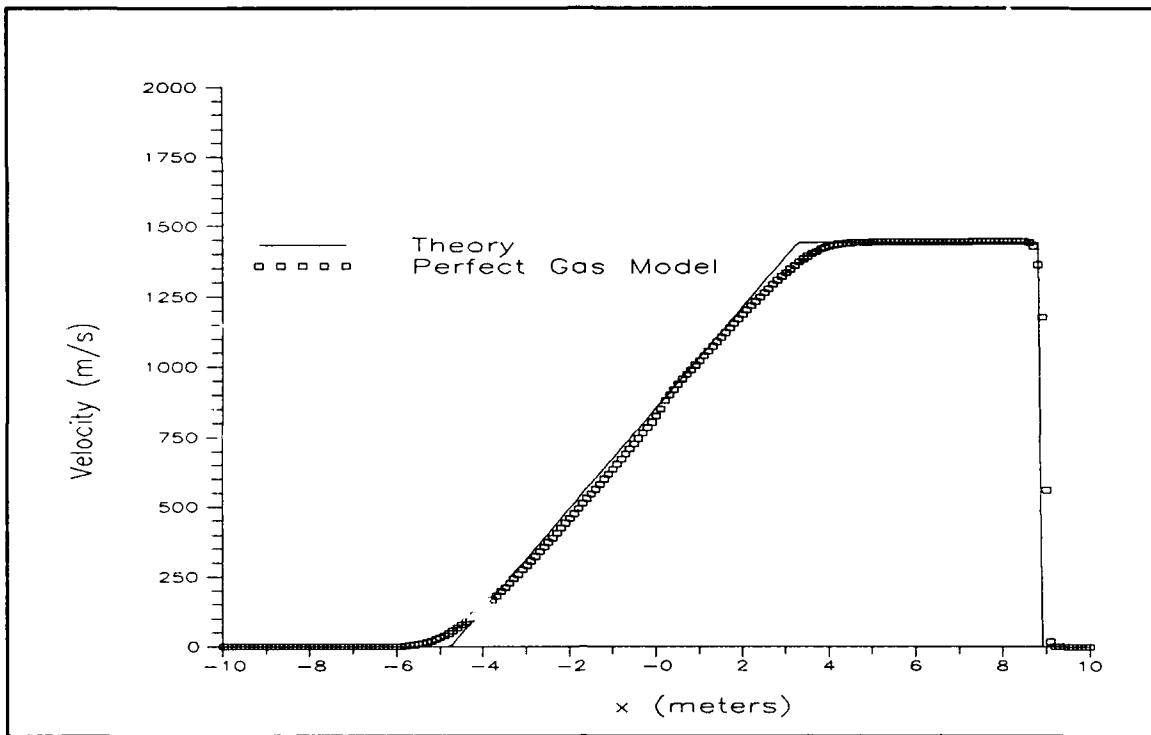


Figure 4 Velocity Profiles for Perfect Gas Model Applied to Shock Tube

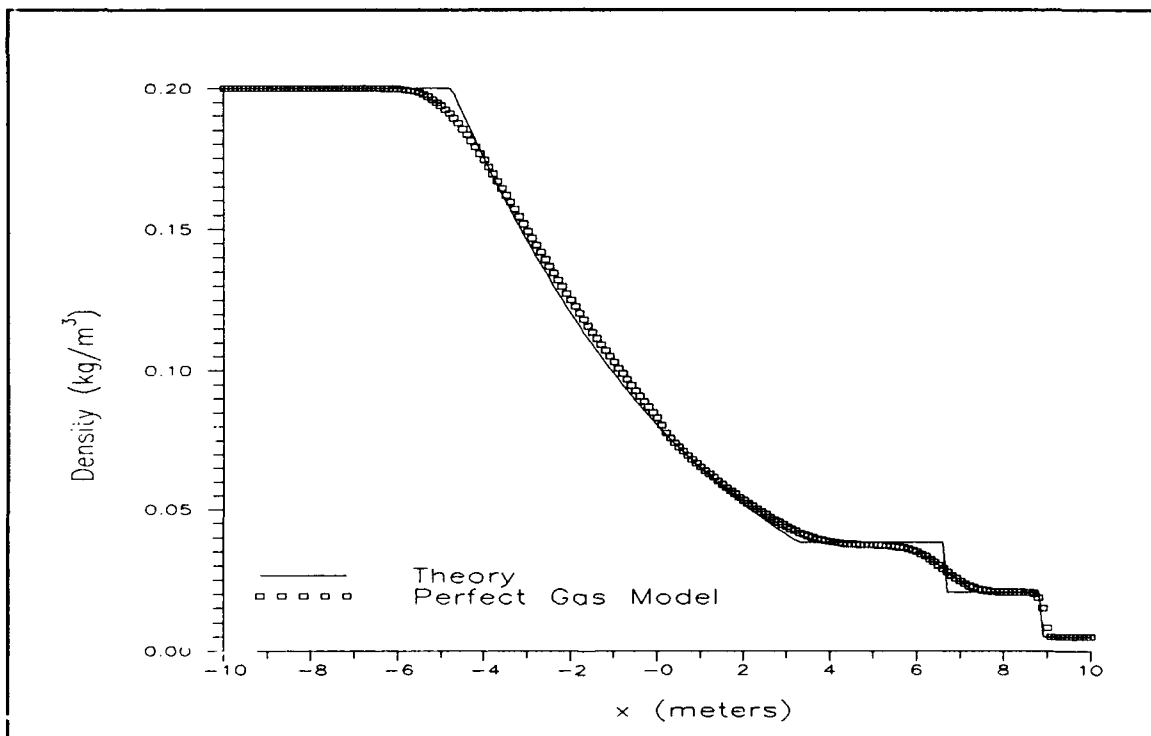


Figure 5 Density Profiles for Perfect Gas Model Applied to Shock Tube

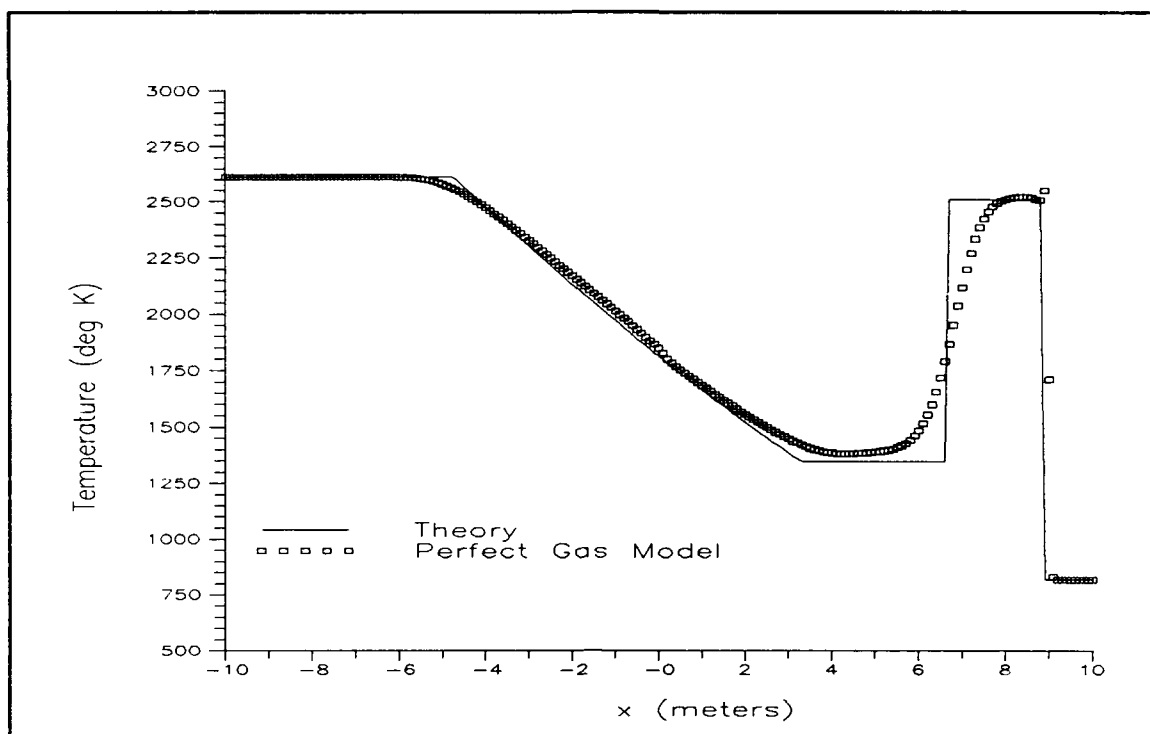


Figure 6 Temperature Profiles for Perfect Gas Model Applied to Shock Tube

The scheme predicted with reasonable accuracy all three flow phenomena (shock, expansion, and contact discontinuity). Furthermore, the scheme smoothly captured the moving shock in only three or four points, which is quite excellent for the strength of the shocks involved. First-order accuracy, however, is apparent from the errors in the expansion fan and contact discontinuity.

An interesting, nonphysical solution appeared in the shock tube numerical simulations. Figure 7 shows a discontinuity within the expansion fan that does not arise in theory or experiment.

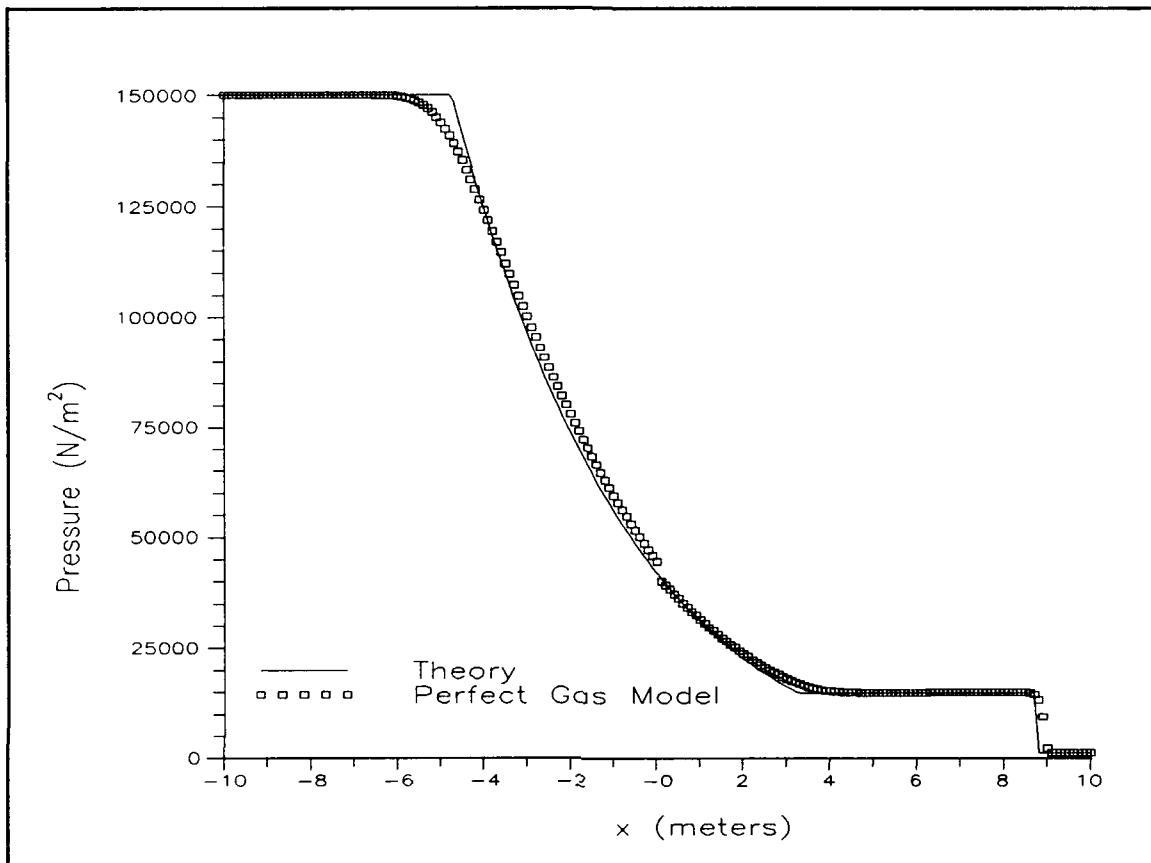


Figure 7 Nonphysical Discontinuity in Shock Tube

This erroneous phenomenon was eliminated by satisfying the "entropy condition for shocks" (10:297-305). The entropy condition is needed to pick out the physically relevant solution, because solutions of hyperbolic conservation laws are not uniquely determined by their initial values (10:297). A small constant parameter, as proposed by Reference 47, was incorporated into the dissipation term and proved sufficient to prevent nonphysical solutions.

## B. Vibrational Effects

Figures 8-12 show the shock tube computations using each vibrational model. The pressure is only nominally effected by vibrational excitation, and changed by about two percent from theoretical predictions (Figure 8).

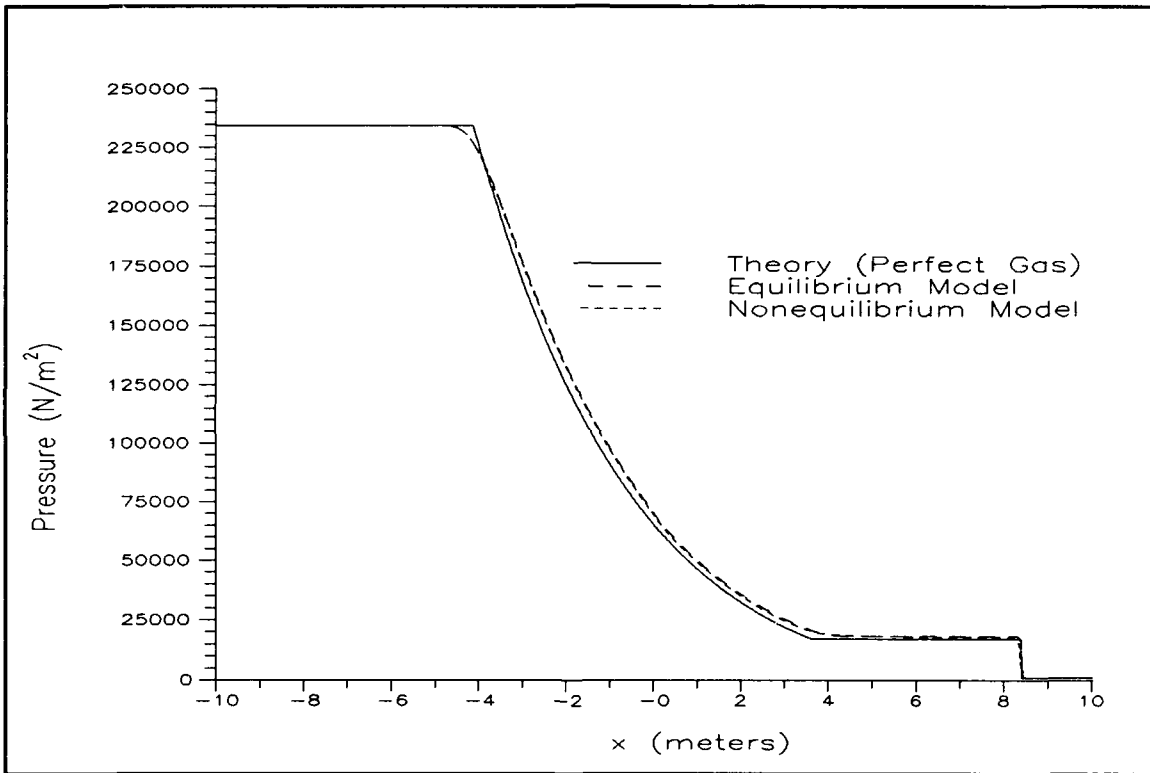


Figure 8      Pressure Profile Comparison for Shock Tube

Temperature and density, however, deviated significantly (10-15 percent) from perfect gas theory (Figures 10 and 11).

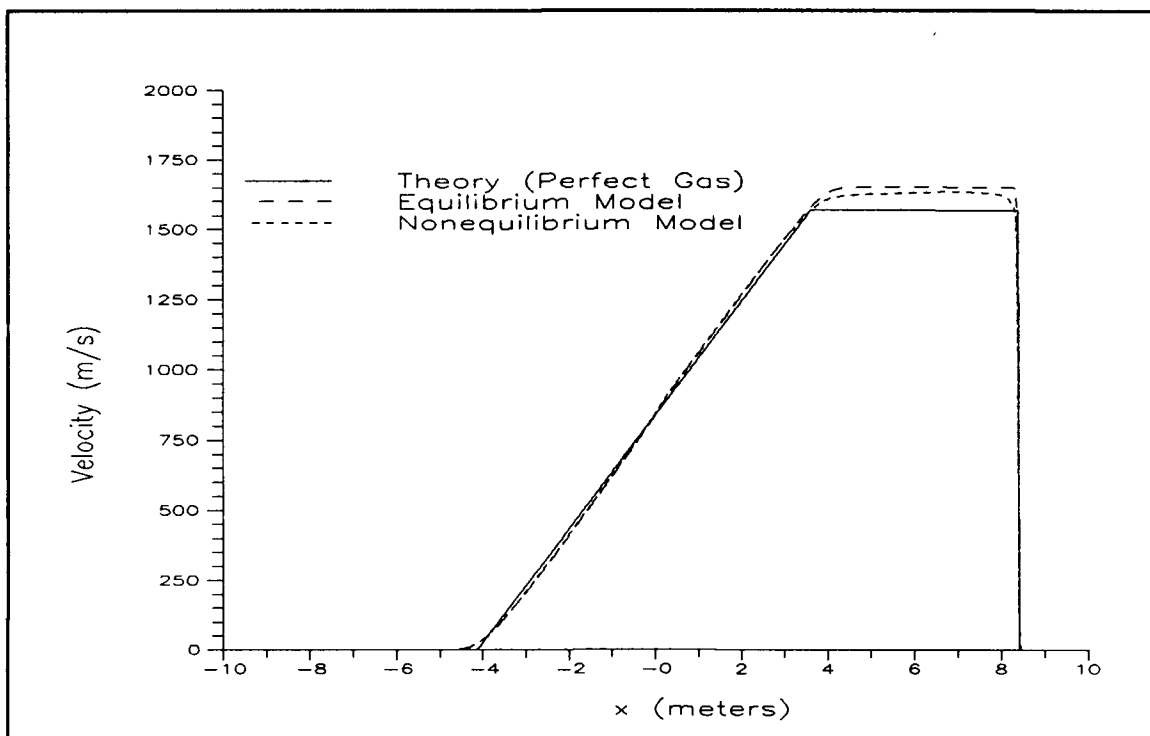


Figure 9 Velocity Profile Comparison for Shock Tube

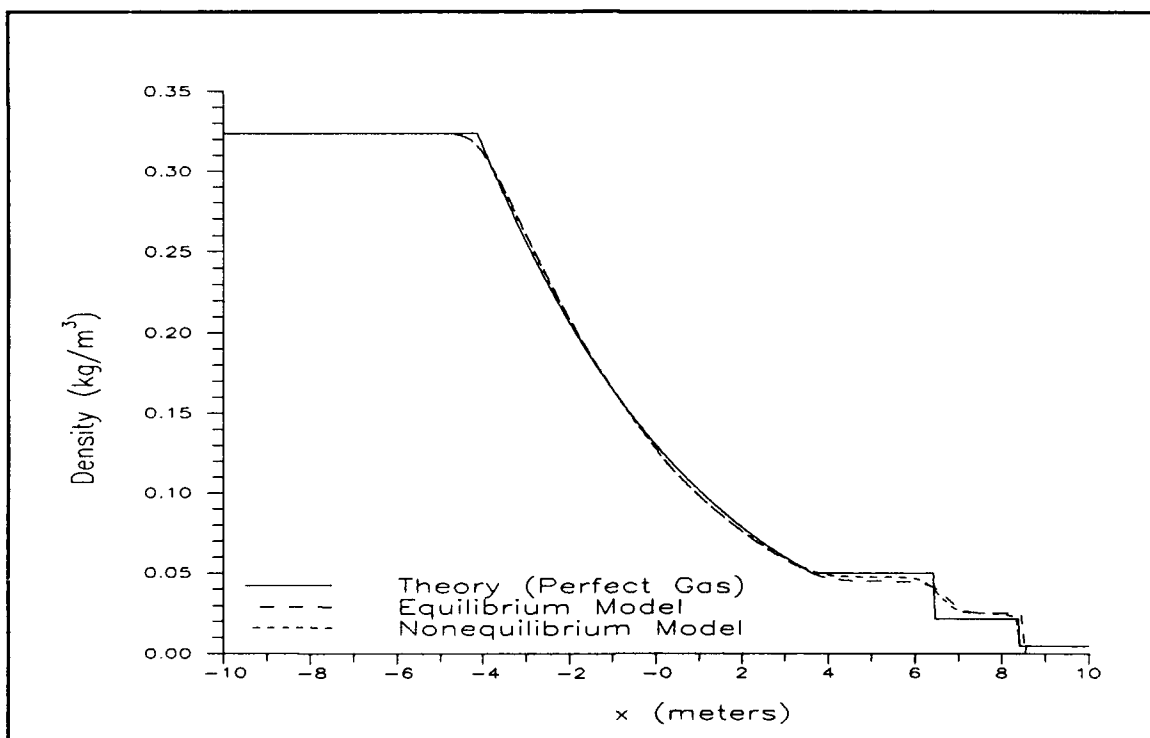


Figure 10 Density Profile Comparison for Shock Tube

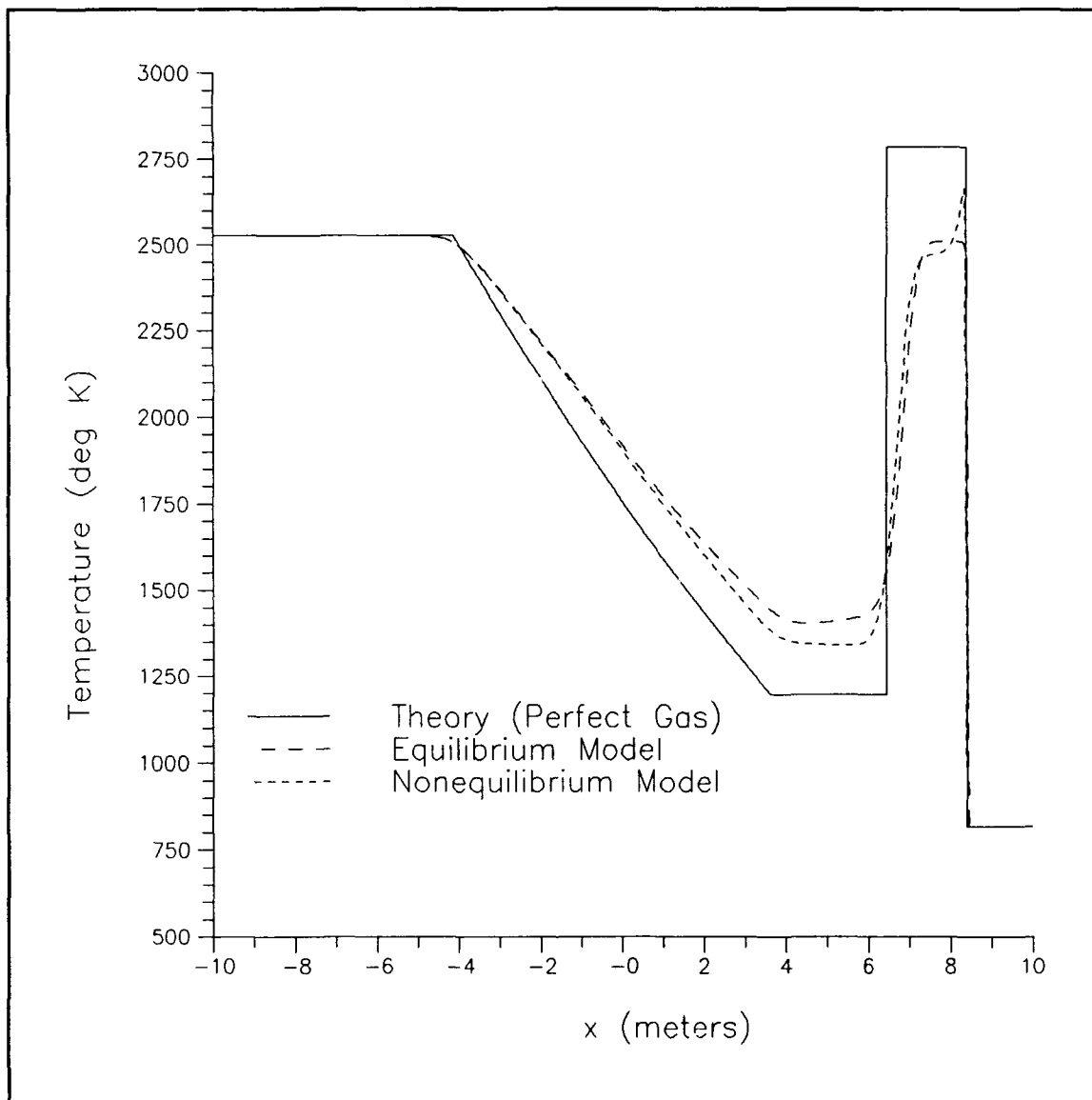


Figure 11      Temperature Profile Comparison for Shock Tube

Figure 12 clearly shows the nonequilibrium relaxation phenomena. The translational/rotational temperature reaches a peak value directly behind the shock, then quickly falls as molecular vibration begins to absorb energy. Equilibrium exists where  $T$  and  $T_{vib}$  are equivalent.

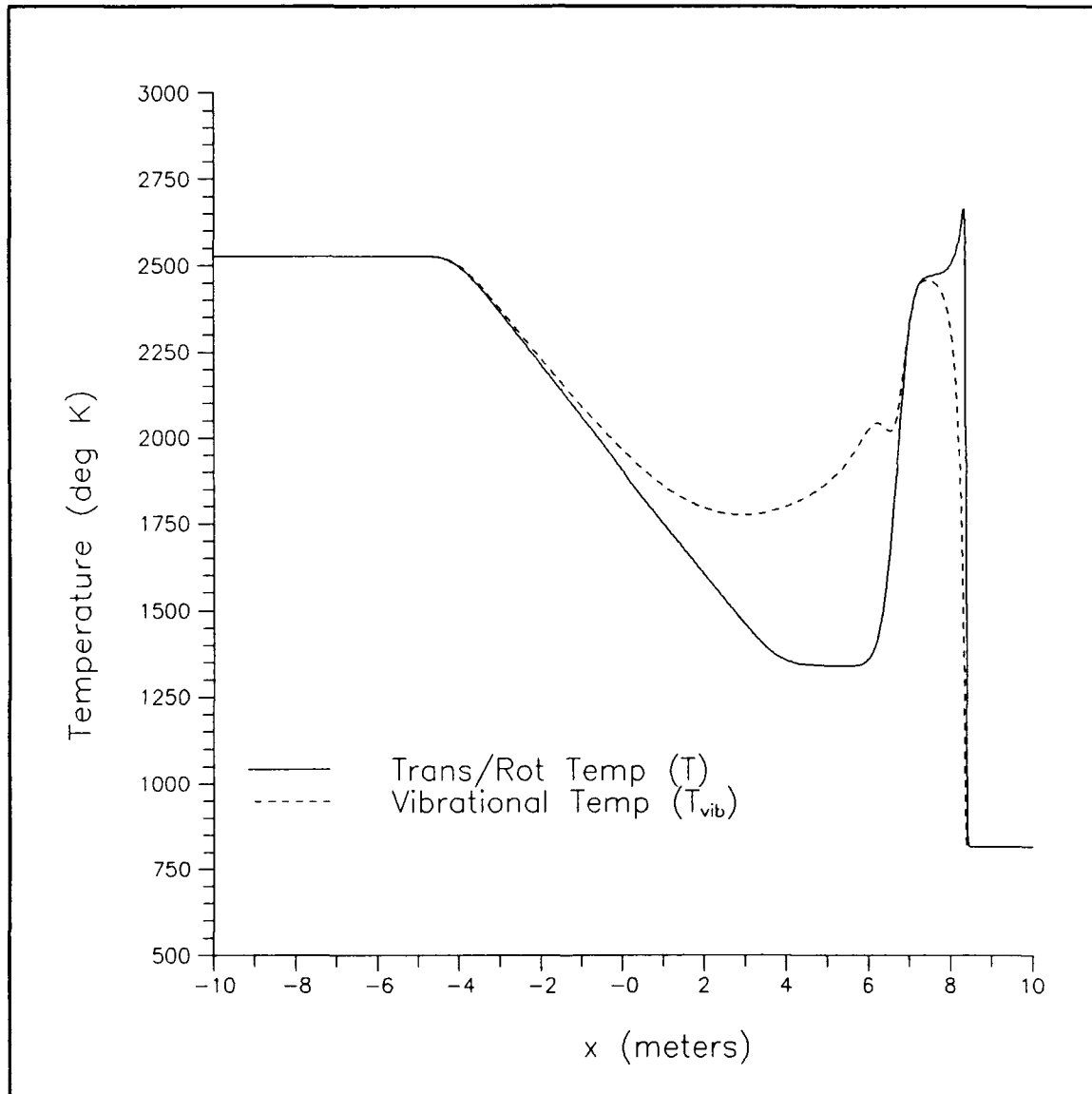


Figure 12      Vibrational Relaxation in Shock Tube

### Density Ratio Calculations

Both qualitative and quantitative comparisons were made with experimental density information. The qualitative comparisons determined the ability of each model to predict the flow features in the shock tube. The quantitative comparison provided a detailed measure of the accuracy.

To make a qualitative assessment of the equilibrium and nonequilibrium models, density interferograms were created from the computed densities at two different conditions. These were then compared to experimental interferograms. The first comparison was for a shock moving at a low Mach number ( $M=2$ ). For this case minimal molecular vibration should take place. The second comparison was for a shock moving at a much higher Mach number ( $M=6$ ). Here molecular vibration is significant. The interferogram is an interference measurement which shows jumps and gradients in the flow field. Gradients appear as curvature in the interference pattern.

Figure 13 (a,b,c) shows the interferograms for  $M=2$ . Both the equilibrium and nonequilibrium models match the experiment and predict a nearly constant density behind the shock. Figure 14 (a,b,c) shows the interferograms for  $M=6$ . Only the nonequilibrium model predicts the relaxation phenomenon shown in the experimental case.



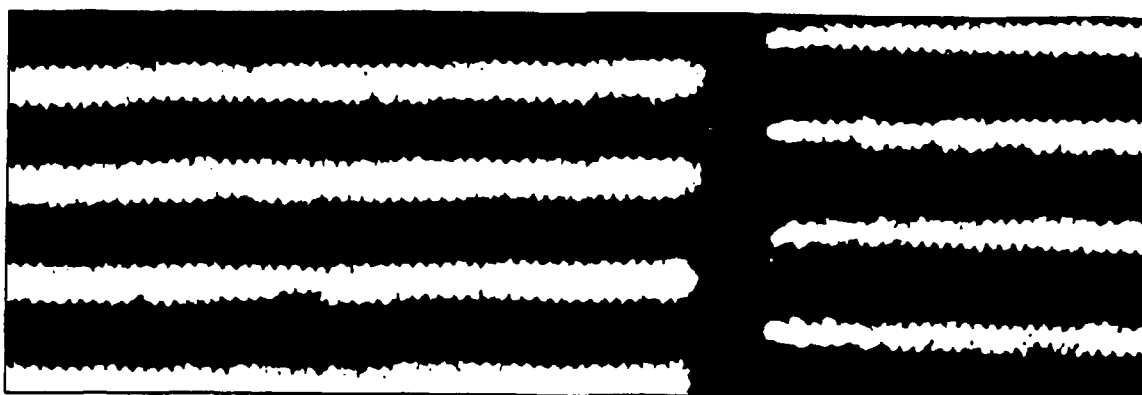


Figure 13a      Experimental Density Interferogram  
(Shock Tube,  $M=2$ )

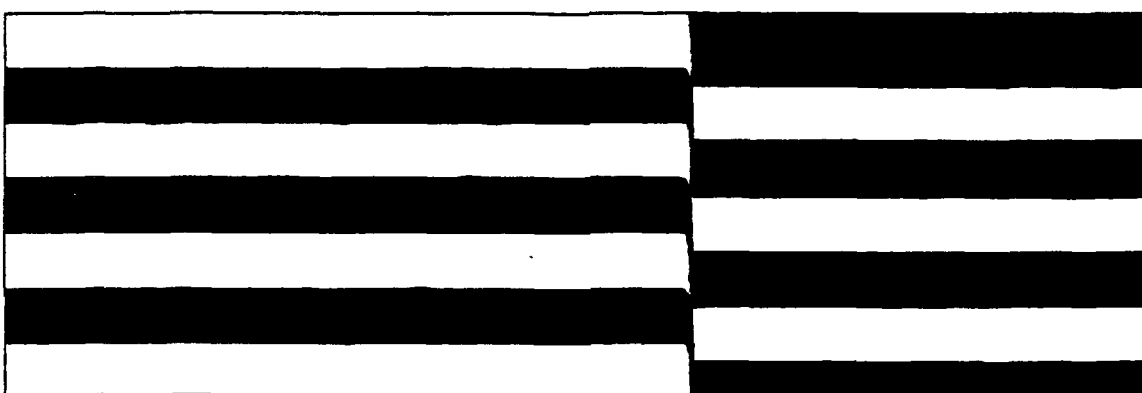


Figure 13b      Nonequilibrium Density Interferogram  
(Shock Tube,  $M=2$ )

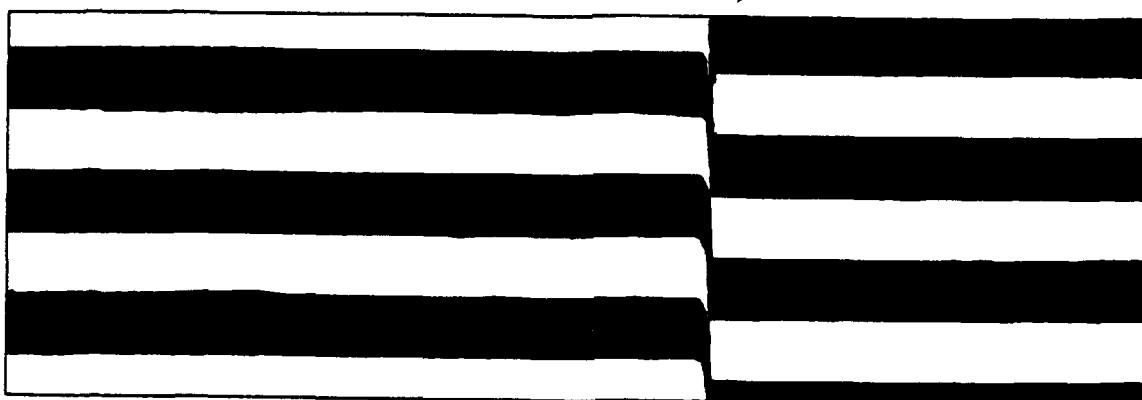


Figure 13c      Equilibrium Density Interferogram  
(Shock Tube,  $M=2$ )

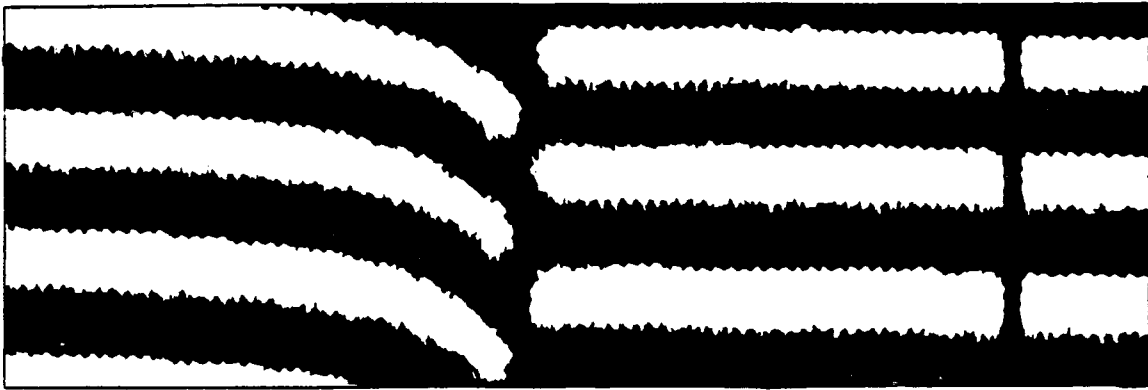


Figure 14a      Experimental Density Interferogram  
(Shock Tube,  $M=6$ )



Figure 14b      Nonequilibrium Density Interferogram  
(Shock Tube,  $M=6$ )

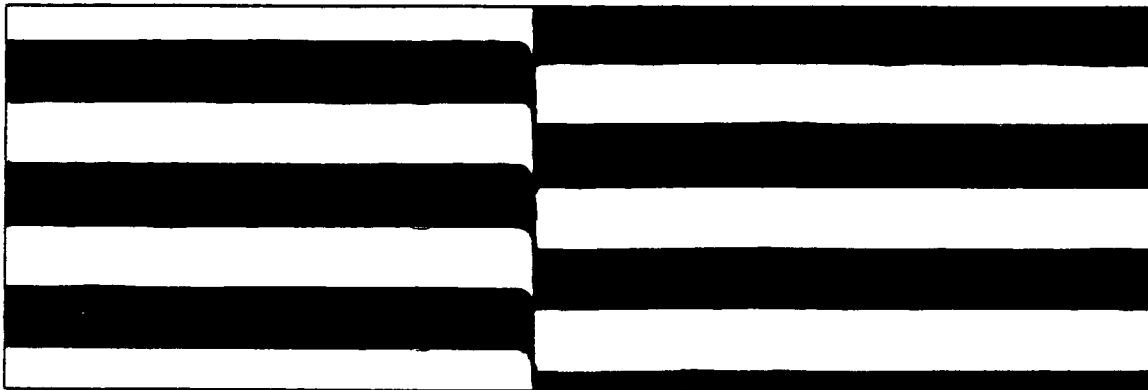


Figure 14c      Equilibrium Density Interferogram  
(Shock Tube,  $M=6$ )

Next more quantitative comparisons were made to fully assess each models validity. To provide a common point of comparison, the densities were calculated after the flow re-equilibrates in the experimental and nonequilibrium cases. The ratios across a normal shock, for both nonequilibrium (relaxing) and equilibrium models, matched the experimental results (3:75-79) for nondissociating air within two percent. Table I summarizes results for a shock wave moving at  $M=5.75$ . Equilibrium may match the experimental results better due to experimental error.

<i>Model</i>	$\frac{T_2}{T_1}$	$\frac{\rho_2}{\rho_1}$	$\frac{P_2}{P_1}$
<i>Theory</i>	7.37	5.21	38.41
<i>Perfect Gas</i>	7.36	5.20	38.36
<i>Equilibrium</i>	7.00	5.80	40.55
<i>Nonequilibrium</i>	6.89	5.84	40.03
<i>Experiment</i>	----	5.75	----

Table I      Calculations across a Moving Shock ( $M = 5.75$ ).

Experimental density ratios for oxygen and nitrogen are plotted in Figure 15 with the results from the nonequilibrium scheme using the Millikan and White model. Clearly, the computations for air follow the experimental trend. Additionally the computed ratios for air fall between oxygen and nitrogen, as one would expect. Recall that the

characteristic vibrational temperature,  $\theta_v$ , used for air (3155 °K ) was a mole-based average of  $\theta_v$  for oxygen(2270 °K ) and  $\theta_v$  for nitrogen (3390 °K ).

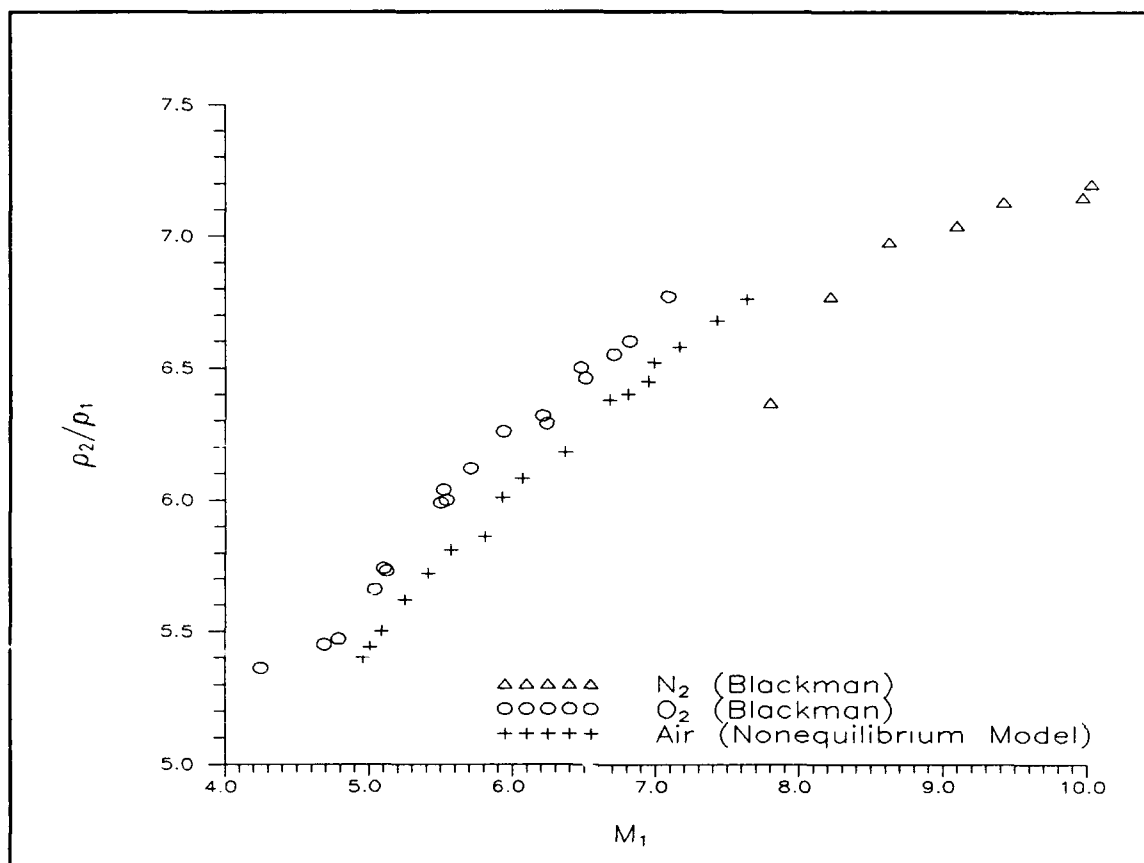


Figure 15 Density Ratios Across a Moving Shock

### Relaxation Times

The relaxation time was computed by observing a stationary point in the shock tube. After the numerical shock passed over this point, time was measured until the flow reattained equilibrium. Figure 16 shows a comparison of

relaxation times for pure nitrogen and pure oxygen, normalized to 1 atm. Relaxation times compared favorably for the range of moderate temperatures (Mach numbers) tested. Although exact agreement was not obtained, quantities computed with the Millikan and White model fall close to the scatter of experimental data.

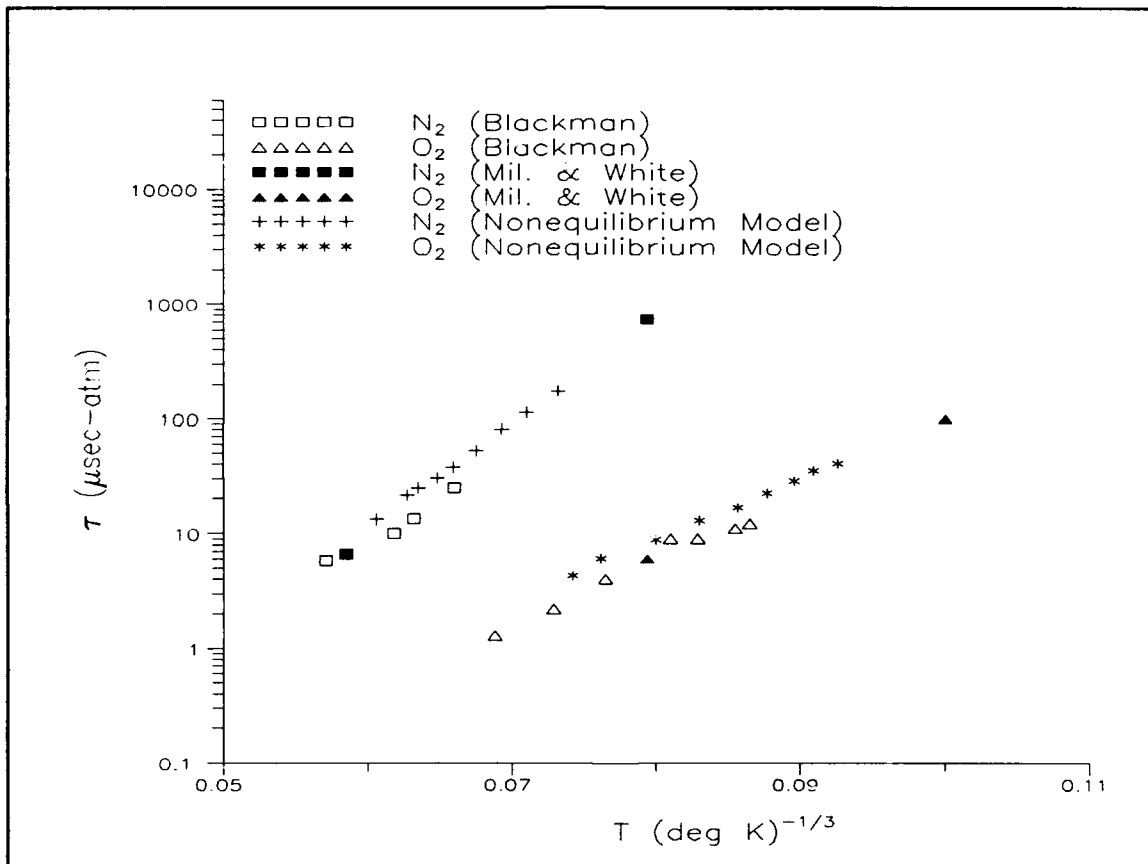


Figure 16 Oxygen and Nitrogen Relaxation Times normalized to 1 atm.

After agreement for pure species was confirmed, mole-averaged constants were employed in the calculations for air as a single, composite species. Figure 17 shows a comparison

of relaxation times between experiment and the nonequilibrium scheme for air with the Millikan and White model. As can be seen, at temperatures below 2500 degrees K, the scheme predicts relaxation rates between pure oxygen and pure nitrogen; much closer to nitrogen. This is consistent with the mole-averaged  $\theta_v$  used. At higher temperatures, the relaxation rates are nearly identical to those of nitrogen.

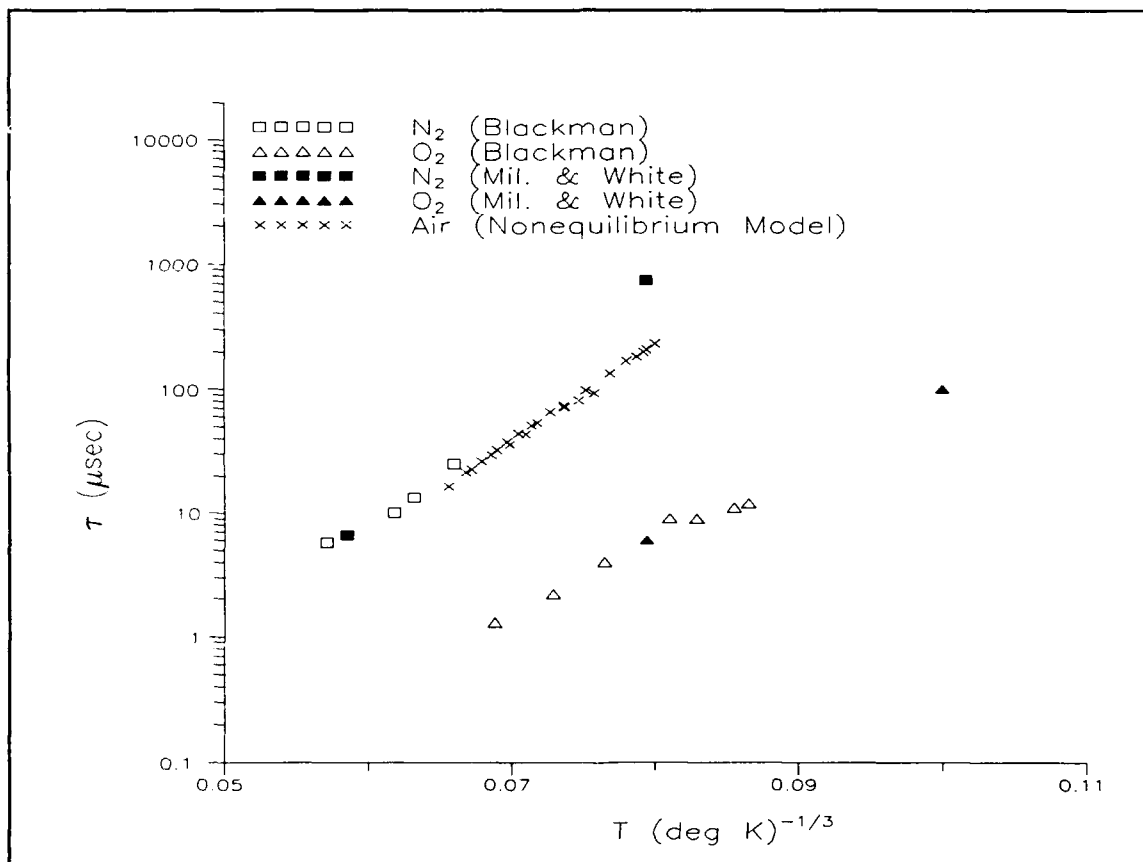


Figure 17 Relaxation Times for Air, Normalized to 1 atm.

Two possible explanations for the models inaccuracy at higher temperatures are a slightly high characteristic vibrational temperature or a failure to account for the dissociative behavior of oxygen at these temperatures. A

characteristic vibrational temperature for air does not explicitly exist. The mole-averaged quantity, derived for this analysis, does not take into account the effectiveness of different collision types, like  $O_2-O_2$  and  $O_2-N_2$ . This significantly impacts relaxation rate prediction as pointed out by Reference 2. Furthermore, oxygen will begin to dissociate above 2300 degrees K.

#### Park Model Versus Millikan and White Model

Only minor differences between the two models could be noted for the temperature range investigated. Table II gives a comparison of results using the Park model and the Millikan and White model.

Temperature (deg K)	Park Model (microsec)	Mil. & White Model (microsec)
3550	21.4	16.4
3350	27.3	21.3
3200	34.1	26.1
3050	40.8	32.2
2950	47.4	37.8
2850	53.9	44.1
2750	59.0	51.5
2600	69.4	65.2
2400	84.3	80.8
2200	186.7	186.5
2050	257.8	257.7
1850	577.0	577.0
1800	668.2	668.2

Table II      Relaxation Times for Two-Temperature Models.

As temperature increased, the Park model calculated longer relaxation times than the Millikan and White Model. This is

consistent with the design of this model. As stated by Park(32:234-235):

The modification accounts for two phenomena that are unique to the high-temperature environment, that is, a limiting value of the cross section and the diffusive nature of vibrational relaxation. The first phenomenon arises from the fact that the correlation formula of Millikan and White implies an unrealistically large cross section for vibrational relaxation at high temperatures. The second correction accounts for the fact that, at high temperatures, vibrational relaxation obeys a diffusion equation with respect to the vibrational energy levels, rather than a Landau-Teller-type rate equation. As a result, the vibrational relaxation rate does not vary linearly with the difference in vibrational energies.

The diverging trend, as temperature increases, is visible in Figure 18.

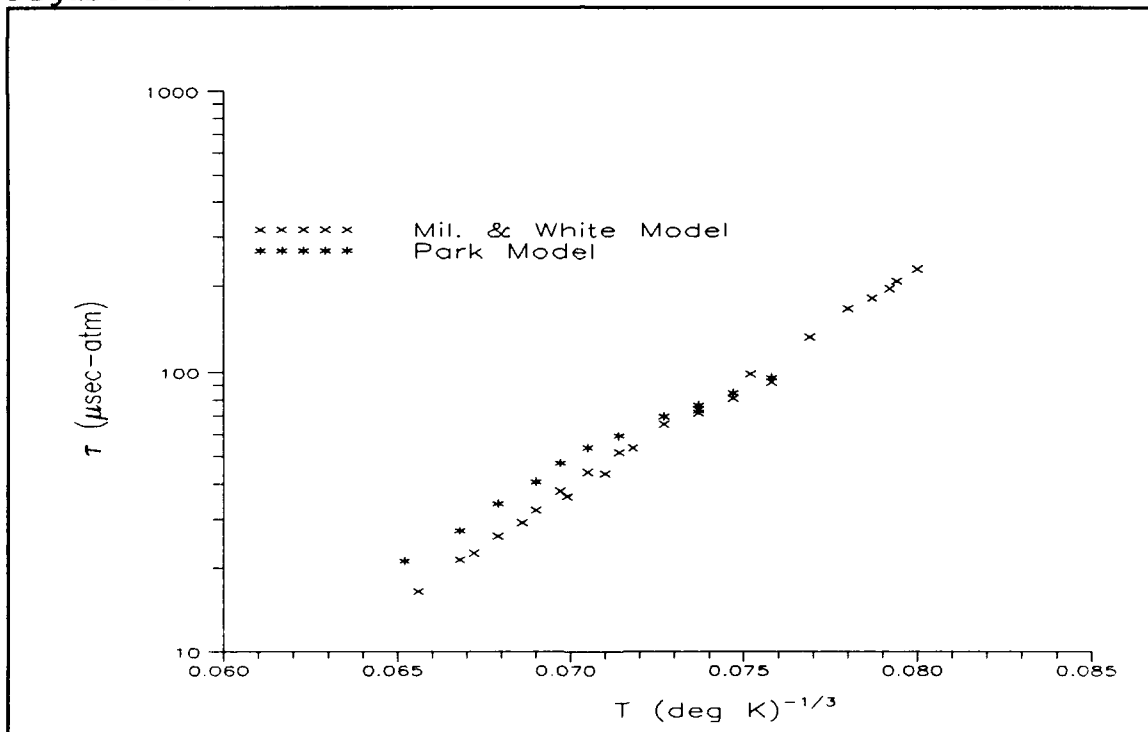


Figure 18 Comparison of Relaxation Times for Two Temperature Models.



No other computational results for the temperature range investigated could be found to confirm these results. However Park developed his model for dissociating and ionizing flows where the mean temperature exceeds 10,000 °K. These results indicate that the Millikan and White model is more accurate at temperatures below 4000 °K. Therefore, for the remainder of this study, only the Millikan and White Model was used.

## V. Blunt-Body Solutions for a Perfect Gas

Solutions of the Euler equations are presented in this section for perfect gas flows about the forward portion of a sphere. Shock standoff distances agreed with experimental results, and sonic line locations agreed with theory. The first-order Roe scheme was very robust to both starting condition and time step while calculating blunt-body solutions. Unfortunately, the algorithm was sensitive to the sphere's geometric singularity and tended to produce oscillations and other nonphysical solutions in the vicinity of the stagnation point. Additionally, some sensitivity to grid refinement was noted.

### A. Solution Flow Structure

Qualitatively, the scheme predicted shock standoff distance, sonic line location, and surface pressure distribution quite well. Figure 19 shows a comparison between experimental and computed shock standoff distances. Tabulated shock standoff distances were taken from References 2,17 and 29. Computed values differed from experiment by about ten percent. This is primarily due to the absence of a boundary-layer in this analysis. A boundary-layer would essentially increase the effective body radius and produce larger shock standoff distances. The trend with increasing Mach number is nicely predicted.

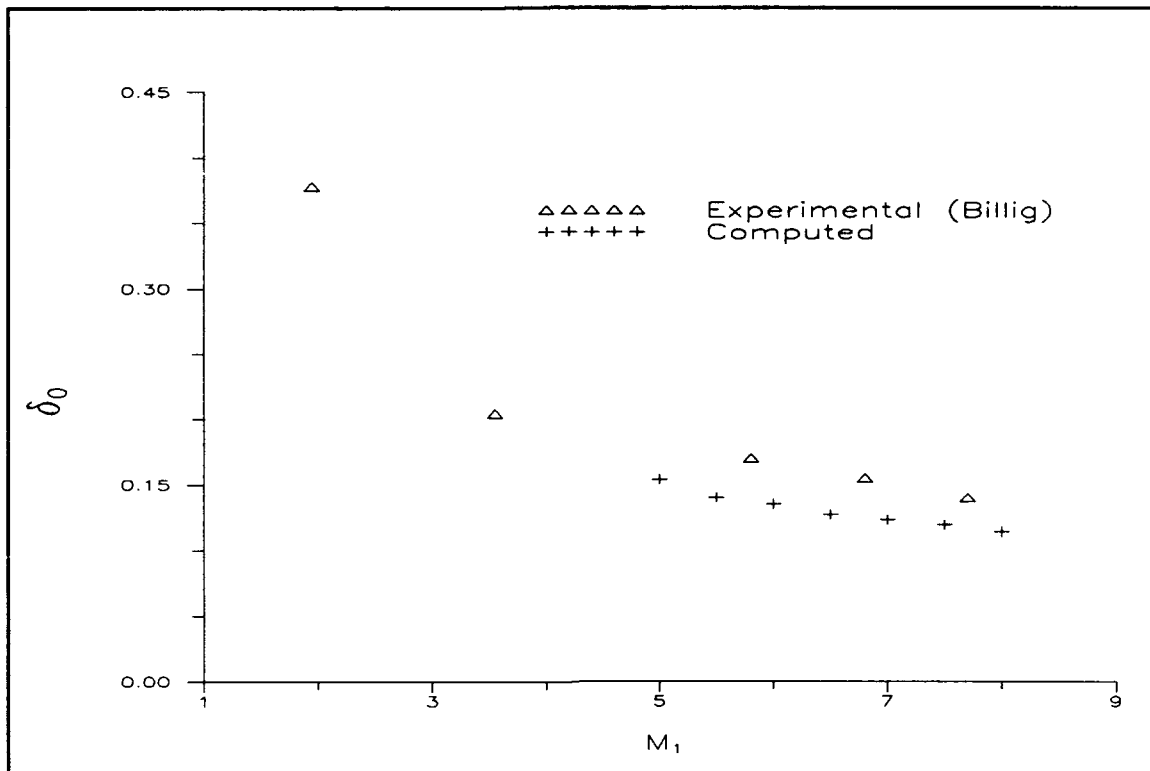


Figure 19 Computed versus Experimental Shock Standoff Distance (Nonequilibrium Model).

The blunt-body calculation also produced accurate sonic line information. In axisymmetric flow, the sonic line should be obtuse to the body at higher Mach numbers (1:184). Figure 20 shows the computed sonic line for a sphere at a freestream Mach number of 7. Additionally the sonic line should be acute for two-dimensional flow. Figure 21 shows the computed sonic line for a cylinder also at Mach 7. These figures indicate that the algorithm predicts the proper physical aspects of the sonic line behavior.

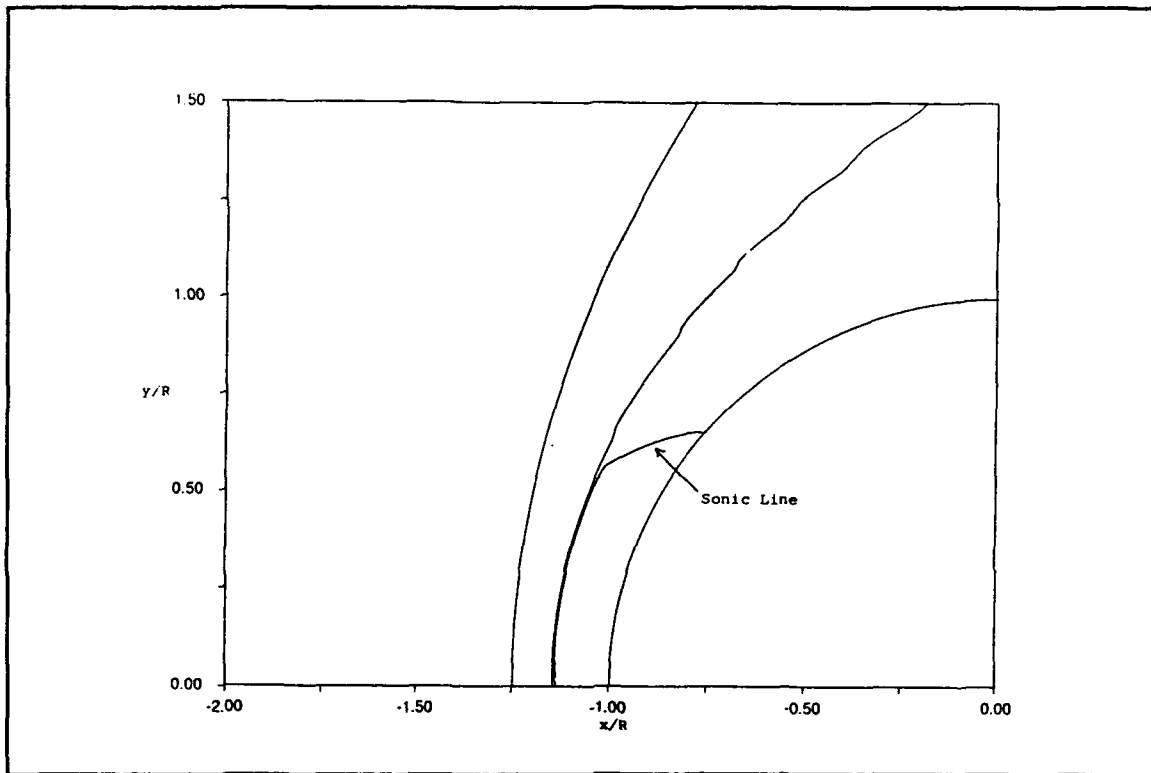


Figure 20 Sonic Line Location for a Sphere at  $M=7.0$

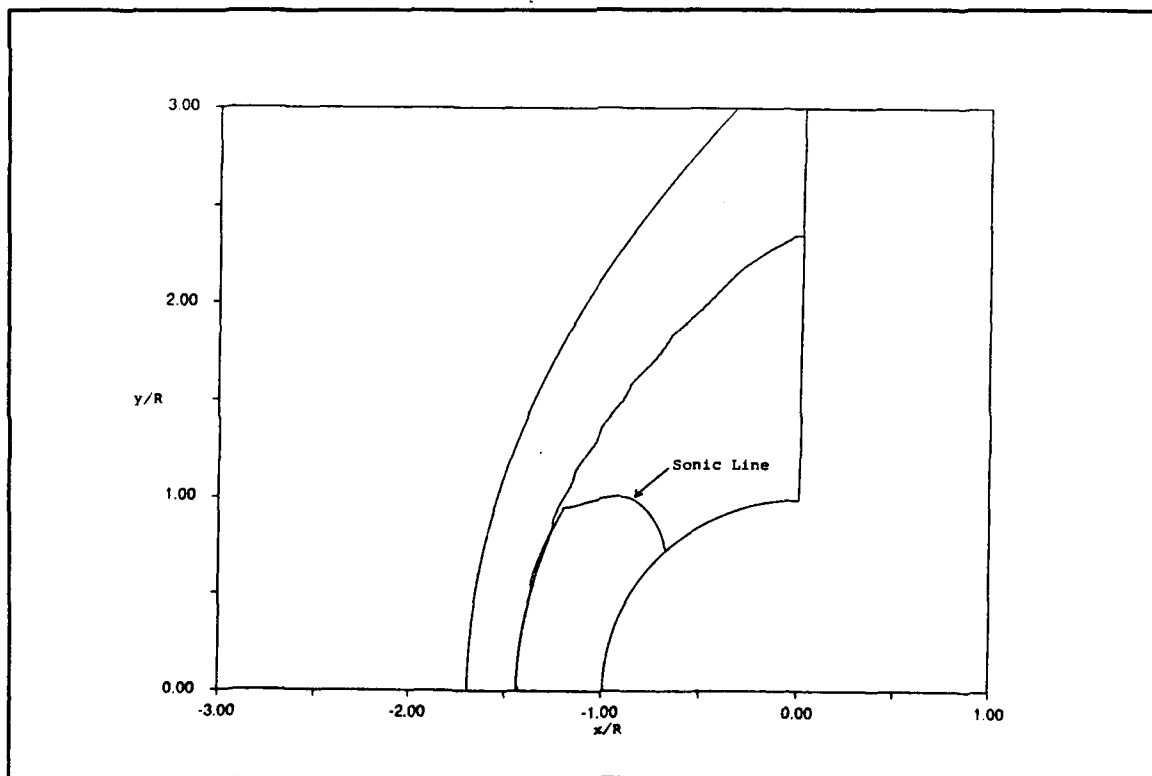


Figure 21 Sonic Line Location for a Cylinder at  $M=7.0$ .

Experimental surface pressure coefficients were extracted from graphical data in Reference 29. The experimental data is plotted in Figure 22 with a modified Newtonian distribution.

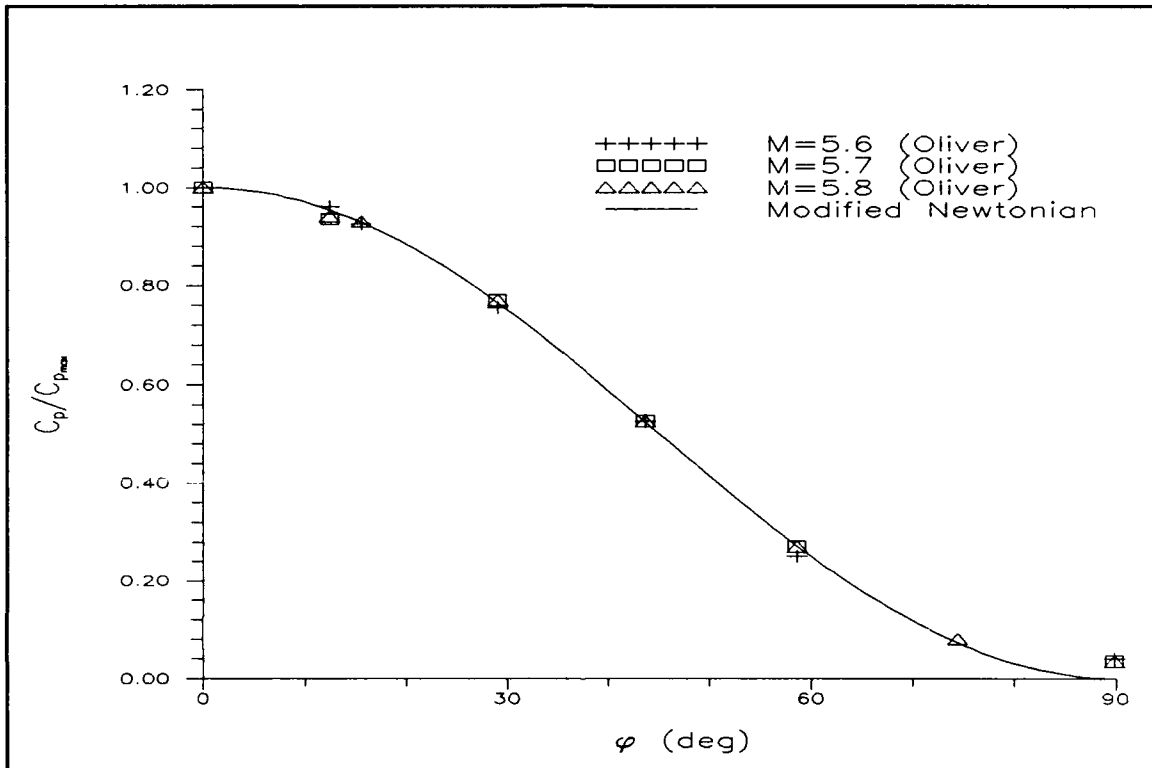


Figure 22 Experimental Pressure Coefficients Around the Forward Portion of Hemisphere Cylinder at M=5.7.

Pressure coefficients from the perfect gas code under predicted experimental data by about five percent. Although the Roe scheme does no better than modified Newtonian, the distribution around the sphere is well predicted (Figure 23), especially at the shoulder. The errors are primarily induced by the algorithm's sensitivity near the symmetry line. This shortcoming is discussed in the next section.

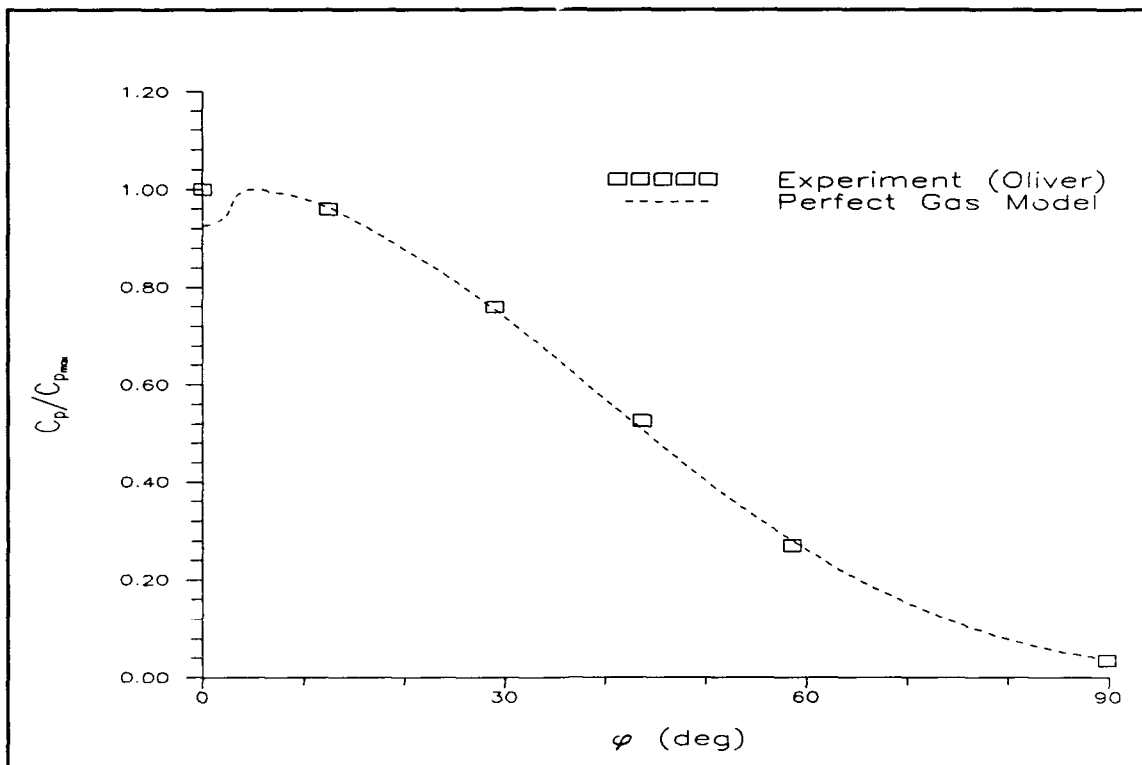


Figure 23 Pressure Coefficients from Perfect Gas Calculations.

## B. Numerical Issues

### Sensitivity Near Symmetry Line

An oscillation near the symmetry line developed in the solution of the axisymmetric problem. The two-dimensional problem did not encounter these oscillations, but similar behavior was observed by Shang and Joshula (39:6). Figure 24 shows Mach contours for flow over a sphere at Mach 5.7; Figure 25 shows similar Mach contours for flow over a cylinder also at Mach 5.7. The solution oscillates, in the axisymmetric case, for the first few degrees from the stagnation line.

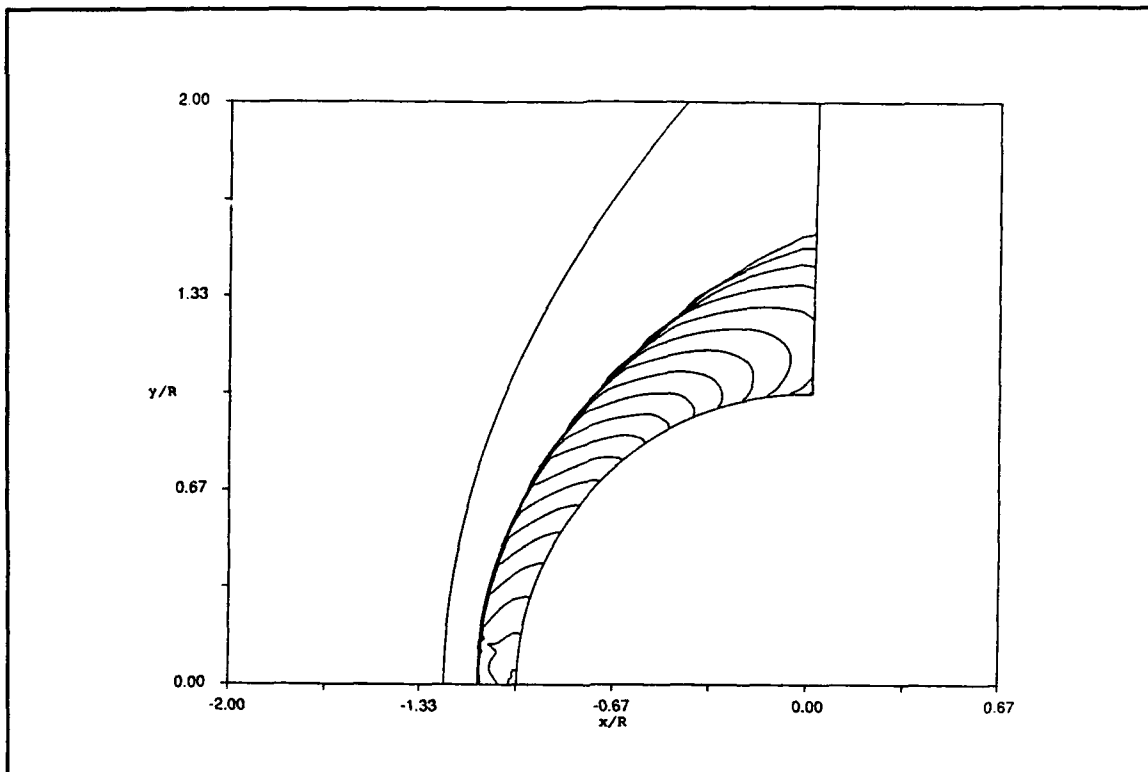


Figure 24 Mach Contours for a Sphere at  $M=5.7$ .

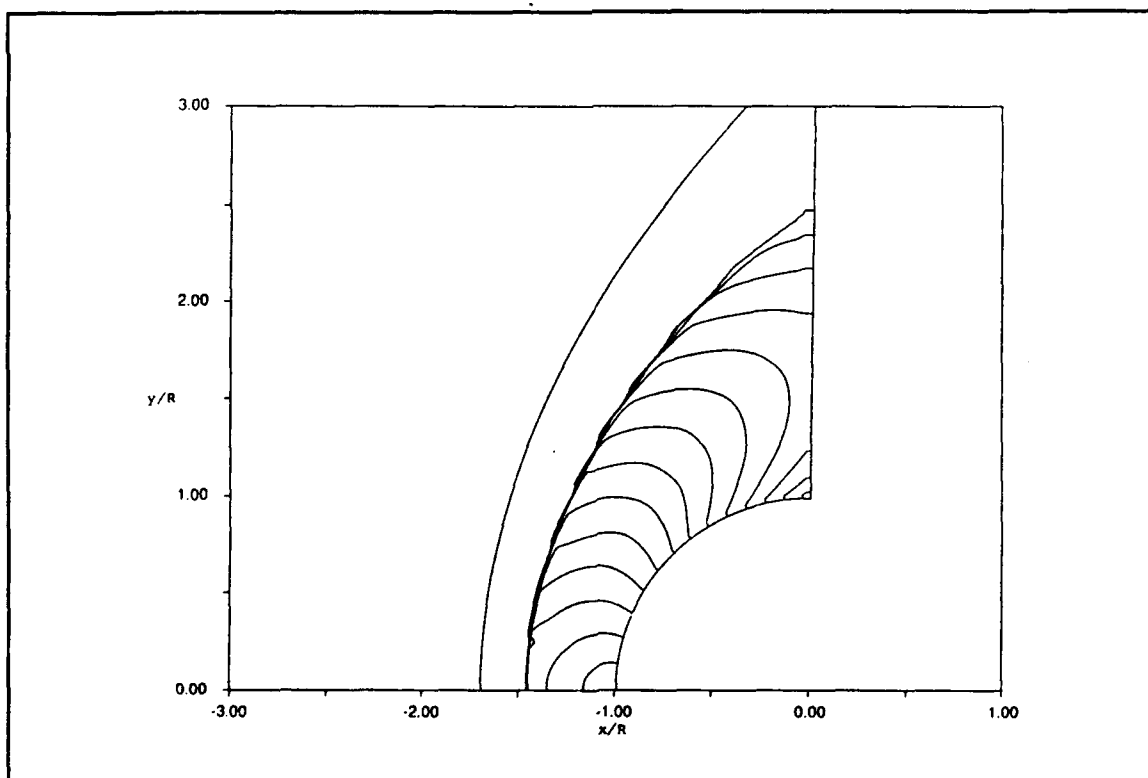


Figure 25 Mach Contours for a Cylinder at  $M=5.7$ .

Figure 26 shows the computed pressure coefficients around a cylinder. Again no oscillations appeared in the 2-D computations.

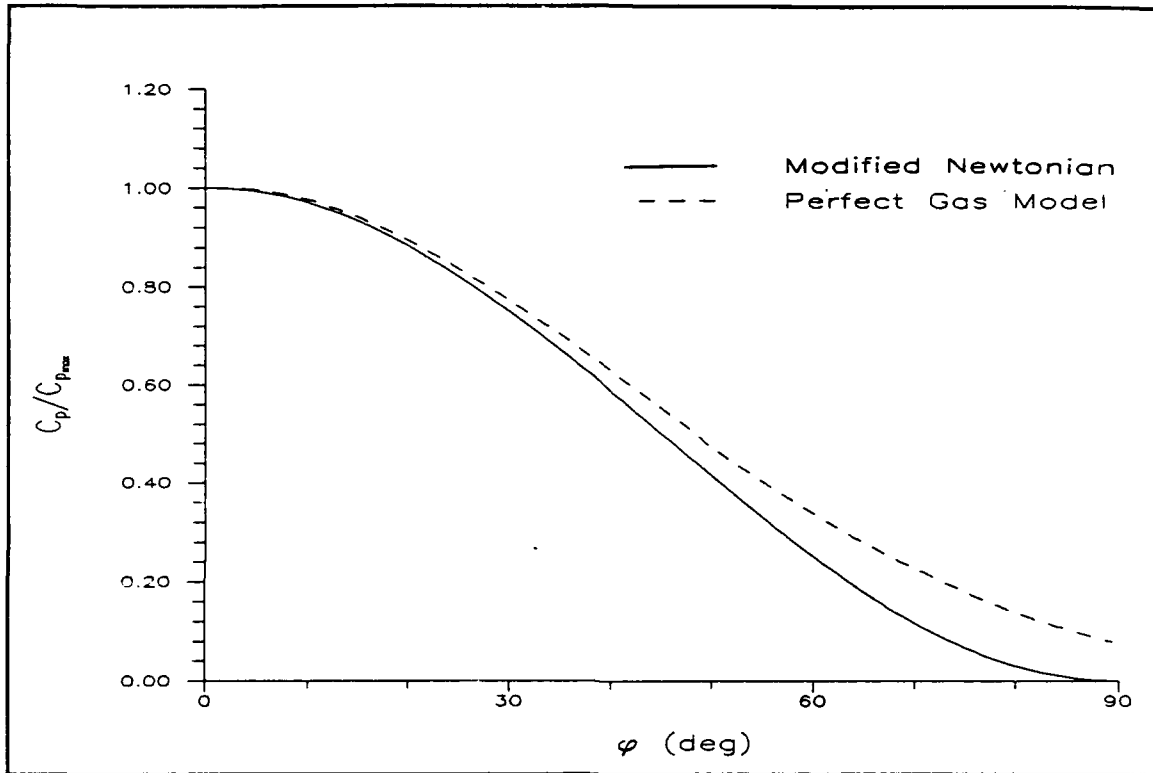


Figure 26 Surface Pressure Coefficients for a Cylinder at  $M=5.7$ .

Studies have shown that proper treatment of numerical boundary conditions has a major impact on the stability of a scheme (47:105). Unfortunately, several variations in the boundary conditions did not improve or eliminate the oscillatory behavior.



The boundary conditions attempted include:

1. Tangency and reflection at the body
2. Tangency and normal momentum at the body
3. Zeroing the fluxes at the symmetry line
4. Vanishing normal derivatives of conserved variables at the symmetry line
5. Utilizing the limiting form for the equations of motion at the symmetry line.

Several other techniques fared no better at improving the solution. These included:

1. Artificial, explicit dissipation near the symmetry line
2. Incorporating an entropy parameter to satisfy the "entropy condition"

Recent work with second-order Total Variation Diminishing (TVD) schemes has shown that limiters and more sophisticated dissipation functions eliminate the oscillatory behavior (47:106). It is important to note that the oscillations were confined to the first five azimuthal nodes, and not to the first few degrees. As the grid was refined, the region effected by the spurious behavior shrank. Therefore, with a refined grid, the integrated affect would be small.

#### Nonphysical Solutions

At the highest Mach numbers tested, a nonphysical recirculation developed in the stagnation region at the shock. This phenomenon is shown in Figure 27. As pointed out by Reference 39, two of the four eigenvalues of the system of equations are zero, therefore initial error will accumulate in the iterative process. This reference characterized the

result as an "accentuated bulge in the shock wave near the axis of symmetry" (39:6). They propose that updating the initial condition may eliminate the error. Attempts to update conditions within the stagnation region did not yield promising results in this study. In theory, the error might be propagated away from this region by using mesh sequencing or limiters in the dissipation formulation (34:6-12).

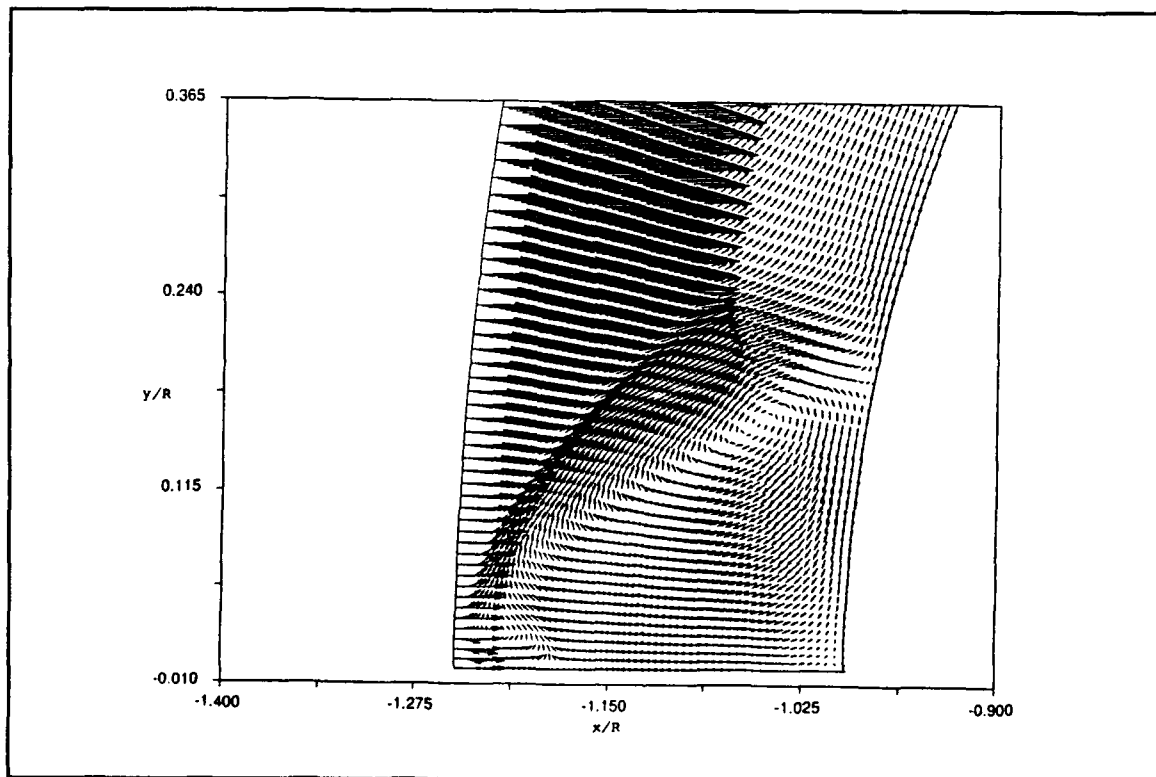


Figure 27 Nonphysical Recirculation Phenomenon in Stagnation Region.

### Grid Sensitivity

The recirculation phenomenon and the grid were highly coupled. As the grid was refined, recirculation occurred at lower Mach numbers. Several permutations in the grid proved unfruitful, including grids which stride the symmetry line and grids which fall on the symmetry line. By maintaining a sufficiently large azimuthal grid spacing near the symmetry line, and a sufficiently large Courant number, the phenomenon could be avoided. Cell aspect ratios of about three to one worked best. Courant numbers between 0.7 and 0.9 provided the necessary dissipation near the shock.

While maintaining the optimal cell aspect ratios, the grid was refined until the shock standoff distance converged. Convergence was determined from the percentage change in shock standoff, and satisfied when this change fell below one percent. A plot of shock standoff distance versus radial node spacing is provided in Figure 28. A coarser grid seems to underpredict the shock layer thickness.

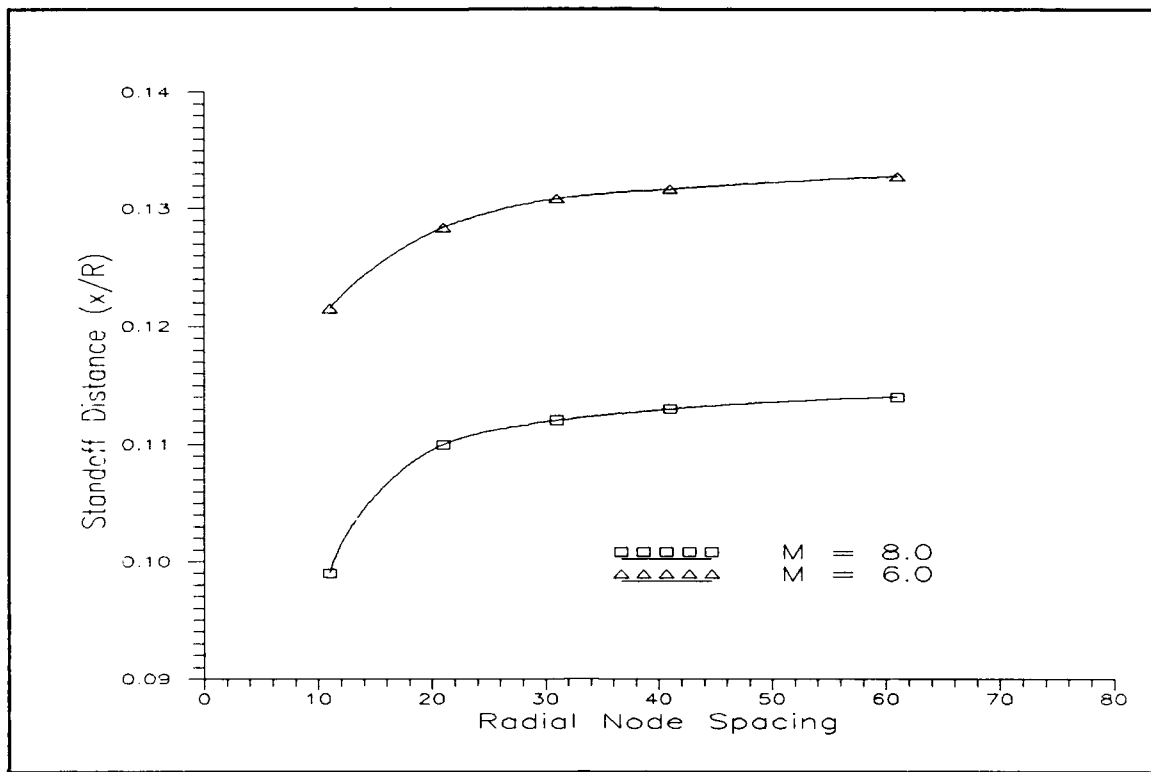


Figure 28      Effect of Axial Node Spacing on Shock Standoff Distance.

## VI. Equilibrium/Nonequilibrium Blunt-Body Solutions

After validating the scheme for the perfect gas model with theory and experimental data, several comparisons to this baseline approach proved illuminating. First, molecular vibration significantly effected shock standoff distance. Second, an interesting low density, high-temperature zone developed immediately behind the shock. Finally, the equilibrium model proved far less robust than hoped.

### A. Shock Standoff Distances

For both the equilibrium and nonequilibrium cases, density increased and shock standoff distance decreased. Density contours for perfect gas and equilibrium airflows over the sphere are presented in Figure 29. A noticeable increase in density and decrease in shock standoff distance can be observed for the equilibrium case. Figure 30 shows a similar temperature contour comparison between equilibrium and nonequilibrium air. As expected, the equilibrium model underpredicts the shock standoff distance. The vibrational relaxation phenomenon is clearly visible in Figure 30. An isolated region of high temperatures forms directly downstream of the shock. As the vibrational states of the molecules become excited and absorb energy, the temperature must decrease. The shape of computed temperature contours, for the

nonequilibrium model, show that temperature is in fact decreasing downstream of the shock.

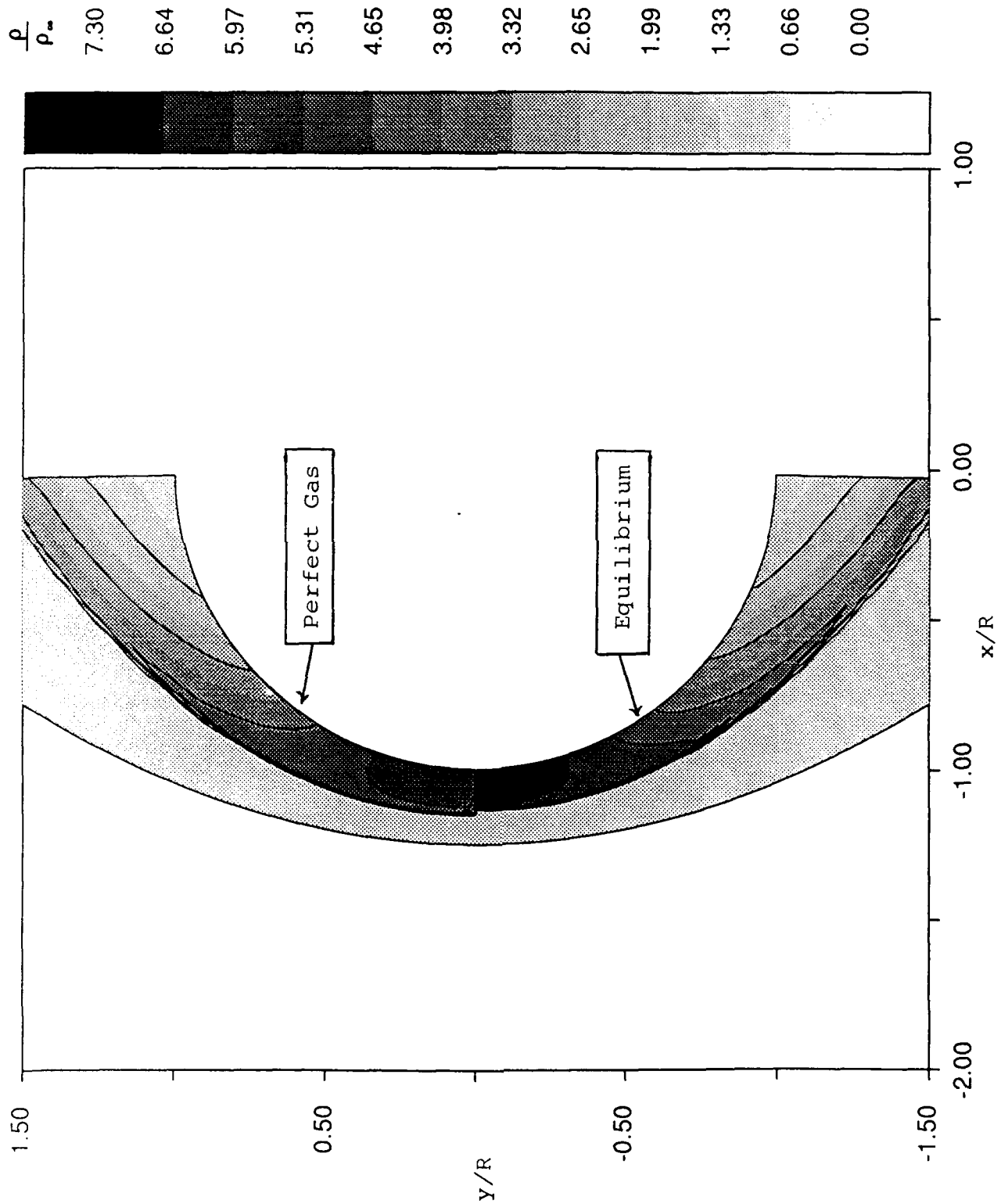


Figure 29 Density Contours for a Sphere at  $M=6.0$

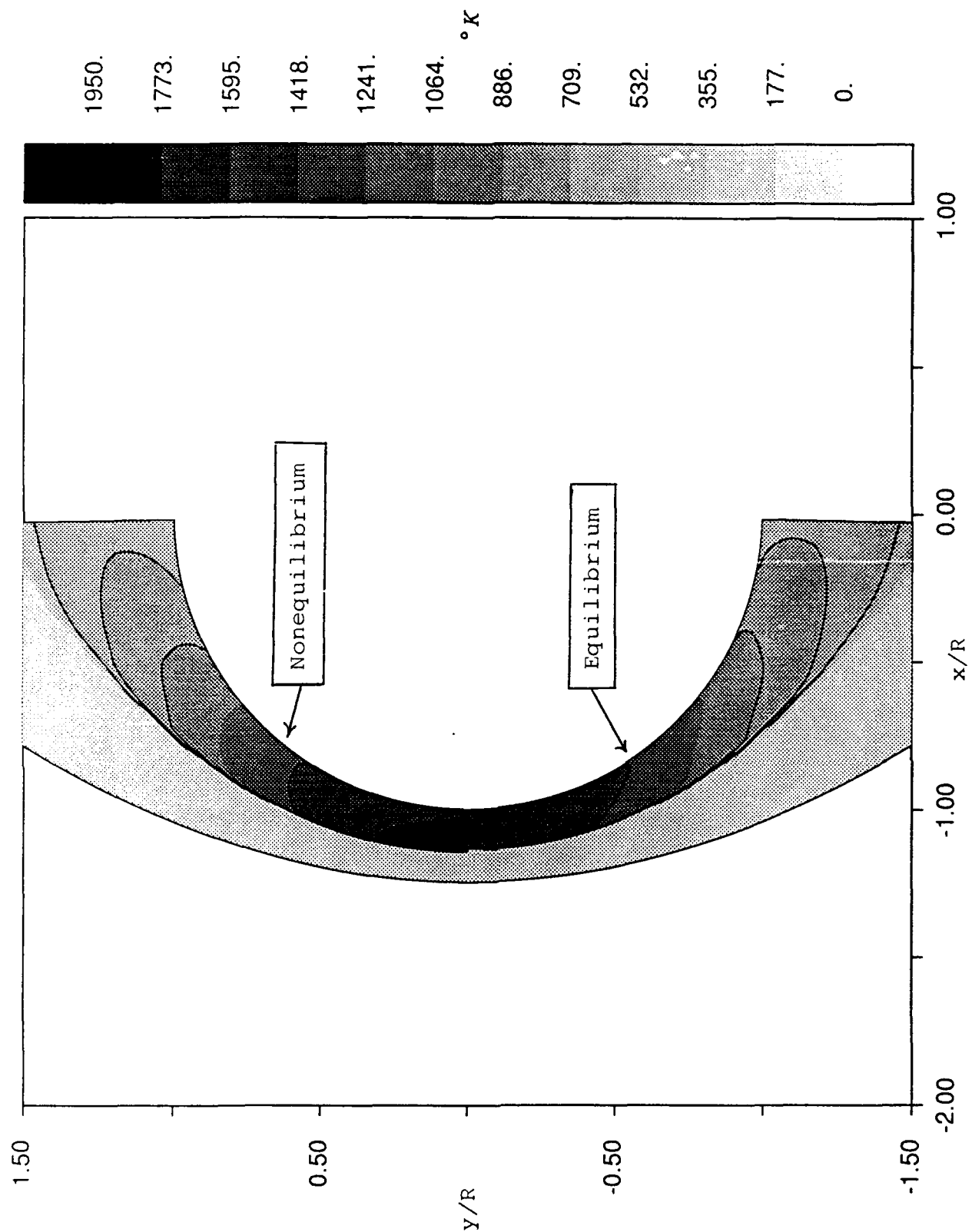


Figure 30 Temperature Contours for a Sphere at  $M=6.0$

As presented in Figure 1, theory predicts that shock standoff distance is linearly proportional to  $\gamma$ . As Mach

number increases, molecular excitation increases, and  $\gamma$  decreases. The nonequilibrium calculations produced changes consistent with this theory for both planar and axisymmetric flow. Figures 31 and 32 show Mach contours around a cylinder (planar flow) for freestream Mach numbers of 5 and 7 respectively. Note the considerably larger decrease in shock layer thickness for the higher Mach number.

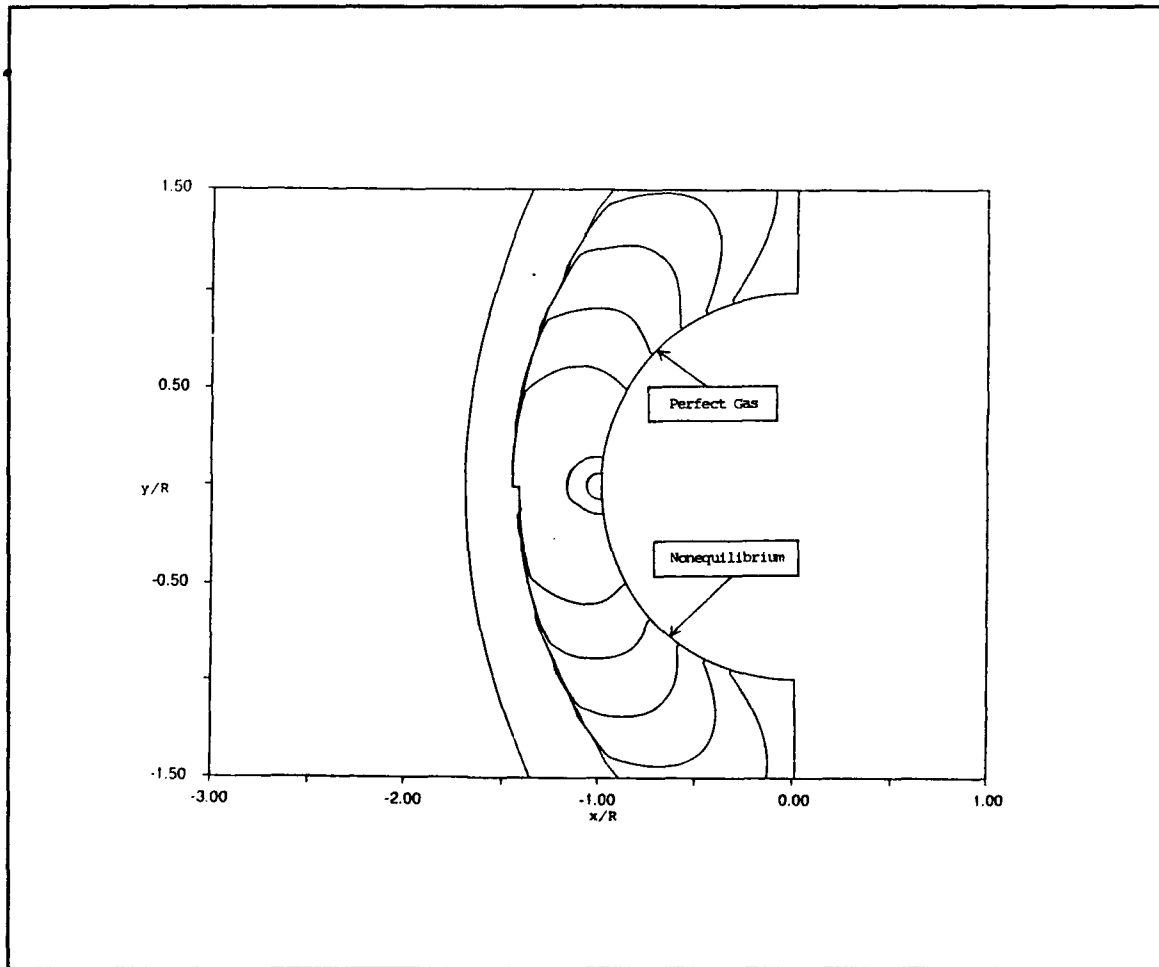


Figure 31      Mach Contours for a Cylinder at  $M=5.0$



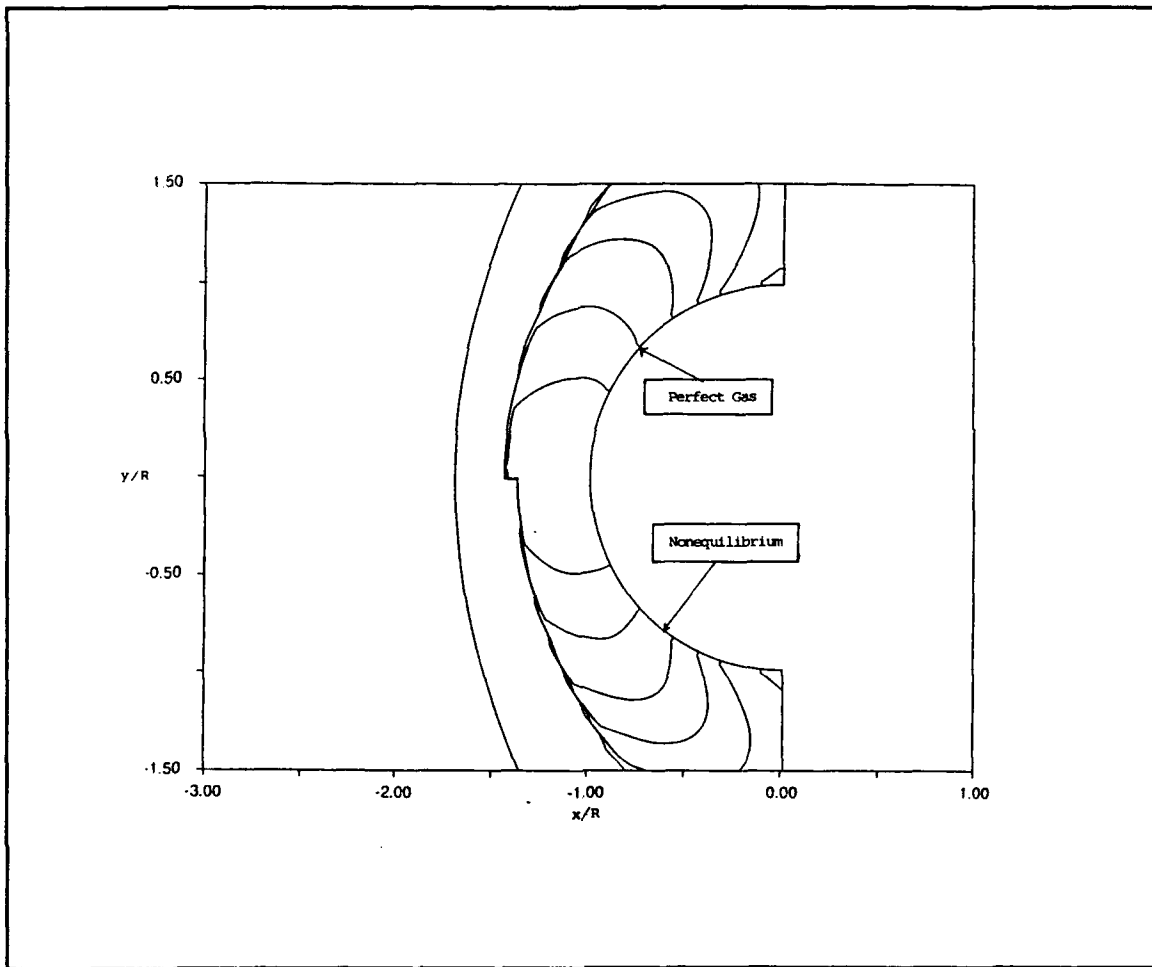


Figure 32 Mach Contours for a Cylinder at Mach 7.0.

The axisymmetric analysis produced similar results. Here, for a freestream Mach number of 6,  $\Delta_0$  decreased by about 7 percent. At a freestream Mach number of 8,  $\Delta_0$  decreased by over 19 percent. If gamma had decreased the same amount for both Mach numbers, the decrease in  $\Delta_0$  would also have been the same. Table III summarizes shock standoff results for a Mach number of 5.7.

<i>Model</i>	$\Delta_o$
<i>Experiment</i>	0.170 $R_b$
<i>Perfect Gas</i>	0.148 $R_b$
<i>Nonequilibrium</i>	0.140 $R_b$
<i>Equilibrium</i>	0.138 $R_b$

Table III      Shock Standoff Distances for Hemisphere Cylinder  
at  $M=5.7$ .

As described earlier, the inviscid scheme underpredicts the shock layer thickness due to the absence of a boundary-layer. Note, however, shock location followed the proper trend as the various models were incorporated. Two physical aspects of fluid motion support this trend. First molecular vibration absorbs energy; therefore, temperature must decrease. Since the pressure is only weakly coupled to the translational energy mode, this molecular vibration will primarily require the densities to be lower. Second, conservation of mass must be maintained. Lower densities require more volume to satisfy consistent mass flow constraints. Both of these principles effect both thermal equilibrium and thermal nonequilibrium, but the nonequilibrium case requires a finite time and distance to accomplish the energy transfer, and will thus have thicker shock layers.

### B. Relaxation in Stagnation Region

Nonequilibrium calculations produced striking temperature and density gradients in the stagnation region, with an isolated "hot spot" near the shock. Figure 33 shows the region of highest temperature located next to the shock. This contrasts with perfect gas and equilibrium calculations where the stagnation point temperature is highest.

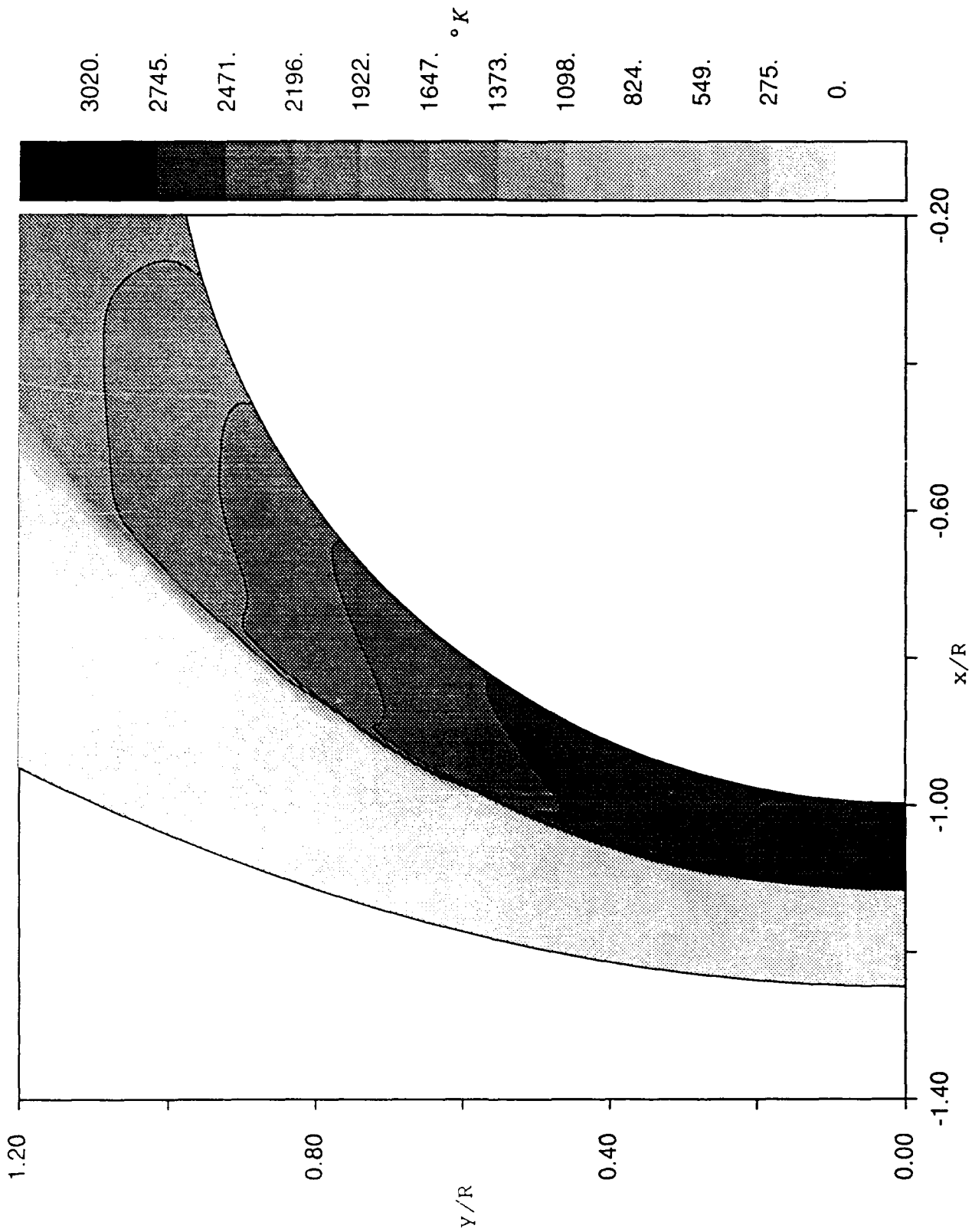


Figure 33 Temperature Contours for a Sphere at  $M=8.0$ ,  
Using Nonequilibrium Model.

Figure 34 shows the translational/rotational temperature plotted against the vibrational temperature along the stagnation line. The flow never quite reattains equilibrium.

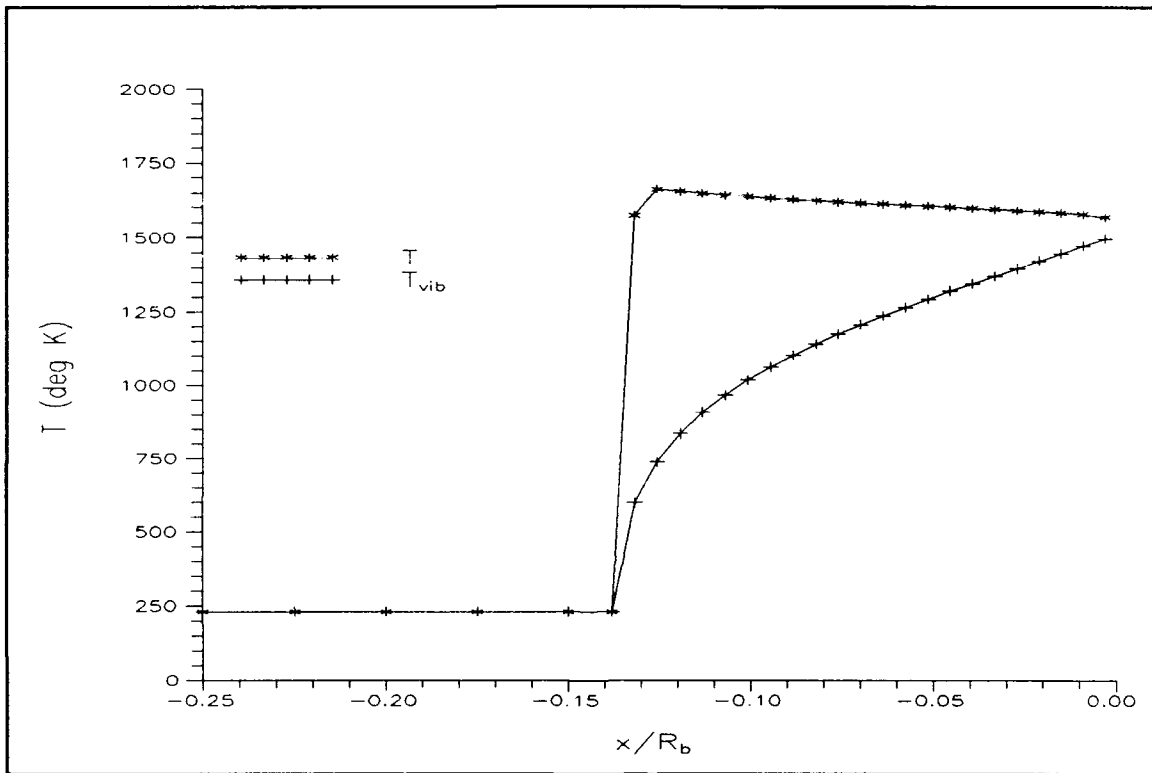


Figure 34 Temperatures Along the Stagnation Line.

The validity of the two-temperature model is questionable at moderate Mach numbers, because the relaxation rates discussed in Chapter 4 differed significantly for comparable temperature ranges. Figure 35 shows the stagnation line vibrational temperatures for pure oxygen and pure nitrogen. The differences throughout the shock layer are quite large.

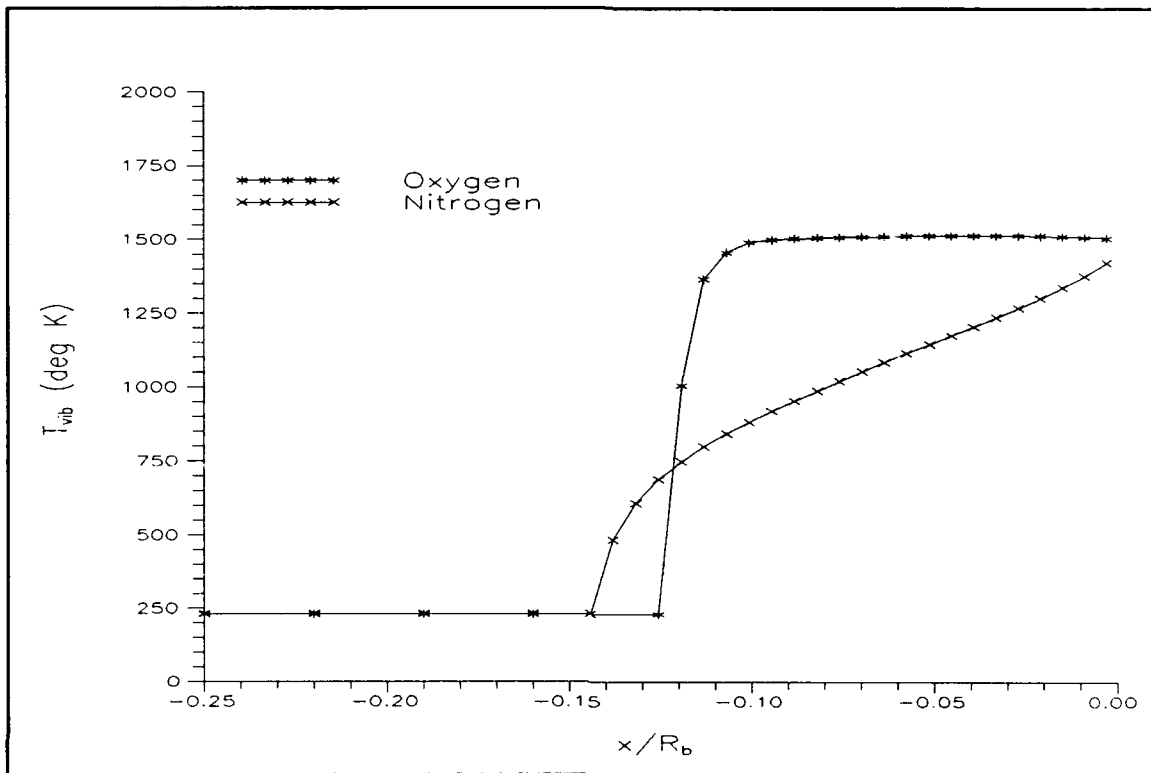


Figure 35 Temperature Comparison within the Shock Layer (Oxygen -vs- Nitrogen).

Surface temperature distributions, on the other hand, did not differ significantly. In fact, the vibrational modeling had little impact on the trend in temperature distribution around the sphere. Figure 36 shows the translational temperature around the sphere for all three gas models: perfect gas, equilibrium, and nonequilibrium. Discrepancies between the magnitudes are apparent, but clearly the geometry dominates the trend.

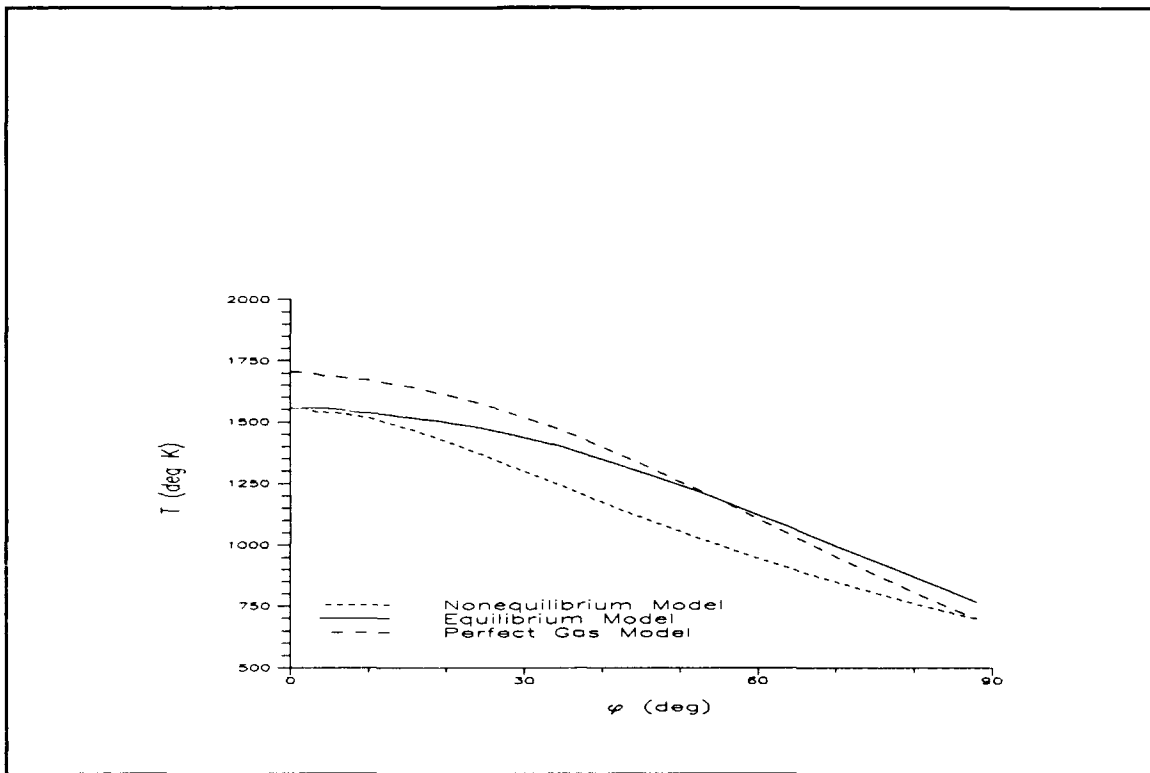


Figure 36 Surface Temperature Distributions for  $M=5.7$ .

### C. Molecular Vibration Model Tradeoffs

The equilibrium model was nearly as complex as both two-temperature relaxing models. The equilibrium model required more CPU time for two reasons. First, a Newton iteration procedure was employed to determine the temperature at each node point. Second, several more parameters had to be "Roe-averaged" to determine the eigenvalues and eigenvectors of the linearized flux Jacobians. Computation times for the code on

a Cray-YMP are summarized in Table IV. No effort was made to fully vectorize the code, so some increase in efficiency could be realized.

<u>Model</u>	<u>CPU Time Required</u>
Perfect Gas	$1.75 \times 10^{-6}$ sec/node pt/time step
Equilibrium	$9.00 \times 10^{-6}$ sec/node pt/time step
Nonequilibrium	$12.30 \times 10^{-6}$ sec/node pt/time step

Table IV CPU Requirements for each Vibrational Model

Equilibrium and nonequilibrium vibrational modeling produced similar surface temperature distributions. At the lowest Mach numbers tested, the differences were less than 15 percent. At Mach 8, the difference shrunk to only 3 percent.

Only nonequilibrium modeling properly captured the radial temperature gradients within the shock layer. This significantly effected proper resolution of temperatures within the stagnation region, especially at or near the shock.



## VII. Conclusions and Recommendations

A first-order Roe scheme was developed for inviscid axisymmetric flows using three different gas models: perfect gas, equilibrium air, and nonequilibrium air. The Roe scheme obtained a converged steady-state solution in about 3000 iterations using an 81 x 41 grid, and a Courant number of 0.9. On the Cray-YMP this took only about 2 minutes. Molecular vibration modeling did not appreciably impact convergence rate. This robustness is impressive in spite of the complications associated with the axisymmetric equations of motion. The scheme's utility for producing reasonable preliminary solutions is certainly supported by the results of the present effort.

The perfect gas model predicts the proper qualitative trend in shock standoff distance, for inviscid flow over a sphere. By incorporating an equilibrium vibration model, both shock standoff distance and temperature decrease by about 10-20 percent.

Changing thermal states near the shock were determined using nonequilibrium modeling. By calculating these rapidly changing thermal states, the nonequilibrium model predicted the highest temperature, and lowest density near the shock.

#### A. Solution Sensitivity to Axisymmetric Equations of Motion

Since the 2-D investigation did not encounter any spurious oscillations, this anomaly is unique to the axisymmetric problem. For the axisymmetric configuration there is a geometric singularity and the Jacobian vanishes along the axis of symmetry. The oscillatory behavior did not affect the final steady-state solution. In fact, the noise near the symmetry line could be filtered out using post-processing. Therefore the behavior was not considered to be a serious determinant to this analysis.

Nonphysical recirculations were avoided by constructing a grid with azimuthal spacing obtained through trial and error. No concrete justification for this can be offered. More investigation into this phenomenon is warranted.

#### B. Accuracy Versus Computational Complexity

The Millikan and White model accurately predicts relaxation rates for the flight regime analyzed. The Park model has several coefficients which could be modified to bring it into closer agreement with the experimental data used in this study. Due to its simplicity the Millikan and White model is preferred. However, if the models are used over a greater variation of Mach numbers, the Park model may prove more accurate at the higher Mach numbers (5:7,32:234).

Since a flow in thermal nonequilibrium develops a "hot spot" just downstream of the shock, for moderate Mach numbers, equilibrium may not be reached in the stagnation region. Moreover, moderate Mach numbers pose a unique problem for the "two-temperature" model. At lower temperatures (i.e. lower Mach numbers), the vibrational temperatures for oxygen and nitrogen at the body surface are significantly different. At higher temperatures (i.e. higher Mach numbers), equilibrium is attained at the body surface, but magnitudes for nitrogen and oxygen differed by 15 percent within the relaxation zone. These two factors may impact heat transfer calculations and calculations involving chemical reactions at the onset of dissociation.

Equilibrium calculations neglect the relaxation of temperature and density within the shock layer. However, near the body surface equilibrium and nonequilibrium calculations differed by only about 3-5 percent above Mach 6. Therefore, in the absence of dissociation, equilibrium can be used to accurately predict inviscid surface conditions.

Unfortunately, the increase in CPU time required to compute an equilibrium solution is intricately linked with the Roe averaging. This makes it less desirable than the nonequilibrium solution.

### C. Recommendations for Follow-on Study

1. Extension of the thermal nonequilibrium analysis to incorporate a second-order-accurate TVD scheme is an appropriate next step. Here the impact of sophisticated dissipation functions can be assessed.

2. Further analysis of the grid/boundary condition interaction may shed further light on the development of spurious behavior near the symmetry line. Particularly, the limiting form of the equations of motion should be more fully analyzed.

3. More detailed analysis using a multi-temperature model with the Roe scheme would help determine if the two-temperature model is sufficient at Mach numbers between 5-10. The multi-temperature model is outlined in Reference 5, and carried out for Mach 25-28 flows using a Gauss-Seidel line relaxation technique.

4. Extension of first-order, inviscid analysis to first-order viscous analysis. Spurious oscillations may go away by introducing "natural" dissipation into the problem. Additionally, the presence of a boundary-layer should produce more accurate shock standoff distances. Finally, computed heat transfer rates can be compared to experiment to further assess the impact of each molecular vibration model.

## Appendix A: Derivations of Governing Equations

### Perfect Gas/Equilibrium

The equations of motion for 2-D or axisymmetric flow can be written in conservation form as:

$$U_t + E_x + F_y = S$$

where,

$$U = \begin{bmatrix} \rho y^\alpha \\ \rho u y^\alpha \\ \rho v y^\alpha \\ E_t y^\alpha \end{bmatrix} \quad E = \begin{bmatrix} \rho u y^\alpha \\ (P + \rho u^2) y^\alpha \\ \rho u v y^\alpha \\ (P + E_t) u y^\alpha \end{bmatrix}$$
$$S = \begin{bmatrix} 0 \\ 0 \\ P\alpha \\ 0 \end{bmatrix} \quad F = \begin{bmatrix} \rho v y^\alpha \\ \rho u v y^\alpha \\ (P + v^2) y^\alpha \\ (P + E_t) v y^\alpha \end{bmatrix}$$

For 2-D flow  $\alpha$  is 0, and for axisymmetric flow  $\alpha$  is 1. To apply these equations in a general coordinate system of  $\xi$  and  $\eta$ , we use the chain-rule:

$$U_t + \xi_x E_\xi + \eta_x E_\eta + \xi_y F_\xi + \eta_y F_\eta = S$$

$\xi_x, \xi_y, \eta_x, \eta_y$  are the familiar metrics of the transformation. By multiplying through by the Jacobian of the inverse transformation,  $\tilde{J}$ , the equation can be recast into the "strong conservation form."

First,

$$\tilde{J}U_t + \tilde{J}(\xi_x E_\xi + \eta_x E_\eta + \xi_y F_\xi + \eta_y F_\eta) = \tilde{J}S$$

Assuming that the grid is fixed in time,  $\tilde{J}U_t = (\tilde{J}U)_t$ . Also,

$$\tilde{J}\xi_x E_\xi = [\tilde{J}\xi_x E]_\xi - E(\tilde{J}\xi_x)_\xi$$

$$\tilde{J}\eta_x E_\eta = [\tilde{J}\eta_x E]_\eta - E(\tilde{J}\eta_x)_\eta$$

$$\tilde{J}\xi_y F_\xi = [\tilde{J}\xi_y F]_\xi - F(\tilde{J}\xi_y)_\xi$$

$$\tilde{J}\eta_y F_\eta = [\tilde{J}\eta_y F]_\eta - F(\tilde{J}\eta_y)_\eta$$

Note that,

$$(\tilde{J}\xi_x)_\xi + (\tilde{J}\eta_x)_\eta = (\tilde{J}y_\eta/\tilde{J})_\xi + (-\tilde{J}y_\xi/\tilde{J})_\eta$$

$$(\tilde{J}\xi_x)_\xi + (\tilde{J}\eta_x)_\eta = y_{\eta\xi} - y_{\xi\eta} = 0$$

In a similar fashion,

$$(\tilde{J}\xi_y)_\xi + (\tilde{J}\eta_y)_\eta = 0$$

Thus,

$$(\tilde{J}U)_t + [\tilde{J}\xi_x E]_\xi + [\tilde{J}\eta_x E]_\eta + [\tilde{J}\xi_y F]_\xi + [\tilde{J}\eta_y F]_\eta = \tilde{J}S$$

$$(\tilde{J}U)_t + [\tilde{J}(\xi_x E + \xi_y F)]_\xi + [\tilde{J}(\eta_x E + \eta_y F)]_\eta = \tilde{J}S$$

Finally, if we let  $\tilde{U} = \tilde{J}U$  and,

$$\tilde{E} = \tilde{J}(\xi_x E + \xi_y F) \quad \tilde{F} = \tilde{J}(\eta_x E + \eta_y F)$$

Now the governing equations can be written in the form suggested by Viviani and Vinokur:

$$\tilde{U}_t + \tilde{E}_\xi + \tilde{F}_\eta = 0$$

There are two drawbacks to this form. One drawback of this form is that new Jacobian matrices (and consequently  $R$  and  $\Lambda$ ) must be developed, since  $\tilde{U}$  is now the vector of dependent variables and not  $U$ . The more general Jacobian matrices are given by:

$$\tilde{A} = \frac{\partial \tilde{E}}{\partial \tilde{U}} \quad \text{and} \quad \tilde{B} = \frac{\partial \tilde{F}}{\partial \tilde{U}}$$

Since  $\tilde{E}$  and  $\tilde{F}$  are most conveniently expressed in terms of the elements of  $U$ ,  $\tilde{A}$  and  $\tilde{B}$  are also determined by using the chain rule:

$$\begin{aligned} \tilde{A} &= \frac{\partial U}{\partial \tilde{U}} \frac{\partial \tilde{E}}{\partial U} = \frac{1}{\tilde{J}} [\tilde{J}(\xi_x E_U + \xi_y F_U)] \\ \tilde{A} &= \xi_x A + \xi_y B \end{aligned}$$

Similarly

$$\tilde{B} = \eta_x A + \eta_y B$$

The second drawback is that a grid with varying metrics will not conserve the freestream. Consider  $E, F$  constant. This implies  $\tilde{E}$  and  $\tilde{F}$  are constant, if and only if  $y_\eta, x_\eta, y_\xi, x_\xi$  are constant.

The problem can be avoided by simply writing the governing equations in the following form (38:2):

$$\tilde{U}_t + (y_\eta E_\xi - x_\eta F_\xi) + (x_\xi F_\eta - y_\xi E_\eta) = \tilde{J}S$$

The solution can be obtained by two successive sweeps, one in the  $\xi$  direction the other in the  $\eta$  direction. In discretized form, the equation for the  $\eta$  -sweep becomes:

$$\tilde{U}_{ij}^* = \tilde{U}_{ij}^n - \frac{\lambda}{2} [y_{\eta_i} (E_{i+1}^n - E_{i-1}^n) - x_{\eta_i} (F_{i+1}^n - F_{i-1}^n)] + \frac{\lambda}{2} (\hat{D}_{i+1/2,j}^n - \hat{D}_{i-1/2,j}^n)$$

where the dissipation term is added for stability. For the Roe scheme the dissipation term is defined as:

$$\hat{D}_{i+1/2,j}^n = R_{\tilde{A}} |\Lambda_{\tilde{A}}^n| R_{\tilde{A}}^{-1} (\tilde{U}_{i+1,j}^n - \tilde{U}_{i,j}^n)$$

and

$$\hat{D}_{i-1/2,j}^n = R_{\tilde{A}} |\Lambda_{\tilde{A}}^n| R_{\tilde{A}}^{-1} (\tilde{U}_{i,j}^n - \tilde{U}_{i-1,j}^n)$$

The variables used in  $R_{\tilde{A}}$ ,  $|\Lambda_{\tilde{A}}|$ ,  $R_{\tilde{A}}^{-1}$  are found by using the Roe-average at the interfaces  $(i+1/2,j)$  and  $(i-1/2,j)$ . The matrix,  $|\Lambda_{\tilde{A}}|$ , is a diagonal matrix of eigenvalues. The derivation of the linearized matrices is performed in Appendix B. Since the vector of unknowns is still  $\tilde{U}$ , the definition of  $\tilde{A}$  remains the same as discussed above for the strong conservation form.



### Nonequilibrium

Here an equation is included for each species which is not in equilibrium (9:7). The conservation form is again written as:

$$U_t + E_x + F_y = S$$

However, now for a system with say two species, diatomic oxygen and nitrogen for example,

$$\begin{aligned}
 U &= \begin{bmatrix} \rho_{N_2} y^\alpha \\ \rho_{O_2} y^\alpha \\ \rho u y^\alpha \\ \rho v y^\alpha \\ E_t y^\alpha \\ E_{v_{N_2}} \\ E_{v_{O_2}} \end{bmatrix} & E &= \begin{bmatrix} \rho_{N_2} u y^\alpha \\ \rho_{O_2} u y^\alpha \\ (P + \rho u^2) y^\alpha \\ \rho u v y^\alpha \\ (P + E_t) u y^\alpha \\ E_{v_{N_2}} u y^\alpha \\ E_{v_{O_2}} u y^\alpha \end{bmatrix} \\
 S &= \begin{bmatrix} 0 \\ 0 \\ 0 \\ P\alpha \\ 0 \\ W_{v_{N_2}} y^\alpha \\ W_{v_{O_2}} y^\alpha \end{bmatrix} & F &= \begin{bmatrix} \rho_{N_2} v y^\alpha \\ \rho_{O_2} v y^\alpha \\ \rho u v y^\alpha \\ (P + v^2) y^\alpha \\ (P + E_t) v y^\alpha \\ E_{v_{N_2}} v y^\alpha \\ E_{v_{O_2}} v y^\alpha \end{bmatrix}
 \end{aligned}$$

where  $E_{v_s}$  is the vibrational energy of species  $s$ , and  $W_{v_s}$  is the Landau-Teller form for the energy exchange between

translational and vibrational energy modes, also for species s. The expansion for a general coordinate system then precedes as above.

The derivation of the linearized matrices used in the Roe-averaged dissipation term, followed the work of Liu and Vinokur (25). Details are again provided in Appendix B.

## Appendix B: Derivation of Flux Jacobians, Eigenvalues, and Eigenvectors

To study high-temperature effects, Roe's approximate Riemann solver was selected because it is both simple and robust. The "Roe-averaged" state was derived by Roe for a perfect gas (35), and generalized for both equilibrium and nonequilibrium flow by Vinokur and Liu (24,42).

### Perfect Gas\Equilibrium

Consistent with the derivation by Liu and Vinokur the flux Jacobians for perfect gas or equilibrium analysis are as follows:

$$A = \frac{\partial E}{\partial U} = \begin{bmatrix} 0 & 1 & 0 & 0 \\ K_1 - u^2 & (2-\kappa)u & -\kappa v & \kappa \\ -uv & v & u & 0 \\ (K_1 - H)u & H - \kappa u^2 & -\kappa uv & (1+\kappa)u \end{bmatrix}$$

$$B = \frac{\partial F}{\partial U} = \begin{bmatrix} 0 & 0 & 1 & 0 \\ -uv & v & u & 0 \\ K_1 - v^2 & -\kappa u & (2-\kappa)v & \kappa \\ (K_1 - H)u & -\kappa uv & H - \kappa u^2 & (1+\kappa)v \end{bmatrix}$$

where

$$K_1 = \frac{1}{2} (u^2 + v^2) + X$$

$$\kappa = \left[ \frac{\partial P}{\partial(\tilde{e})} \right]_p$$

$$X = \left[ \frac{\partial P}{\partial \rho} \right]_{\tilde{e}}$$

$$\tilde{e} = \rho e$$

For perfect gas flows,  $\kappa$  is equal to  $\gamma-1$  and is constant. Also for perfect gas flows  $X$  is exactly zero.

I used Mathematica to derive the eigenvectors for a general coordinate system by letting  $\tilde{A} = \xi_x A + \xi_y B$  :

$$R_{\tilde{A}} = \begin{bmatrix} 1 & 1 & 1 & 0 \\ u-k_1 c & u & u+k_1 c & -k_2 \\ V-K_2 c & v & v+k_2 c & k_1 \\ (H-k_1 u c - k_2 v c) & \left(-\frac{X}{\kappa} + \frac{u^2 + v^2}{2}\right) & (H+k_1 u c + k_2 v c) & (k_1 v - k_2 u) \end{bmatrix}$$

$$R_{\tilde{A}}^{-1} = \begin{bmatrix} \left( \frac{b_1 + \frac{k_1 u}{c} + \frac{k_2 v}{c}}{2} \right) \left( \frac{-b_2 u - \frac{k_1}{c}}{2} \right) \left( \frac{-b_2 v - \frac{k_2}{c}}{2} \right) \left( \frac{b_2}{2} \right) \\ 1-b_1 & b_2 u & b_2 v & -b_2 \\ \left( \frac{b_1 - \frac{k_1 u}{c} - \frac{k_2 v}{c}}{2} \right) \left( \frac{-b_2 u + \frac{k_1}{c}}{2} \right) \left( \frac{-b_2 v + \frac{k_2}{c}}{2} \right) \left( \frac{b_2}{2} \right) \\ k_2 u - k_1 v & -k_2 & k_1 & 0 \end{bmatrix}$$

where

$$b_2 = \frac{\kappa}{c^2}$$

$$b_1 = b_2 \left[ \left( \frac{u^2 + v^2}{2} \right) + \frac{X}{\kappa} \right]$$

$$k_1 = \frac{\xi_x}{(\xi_x^2 + \xi_y^2)^{\frac{1}{2}}}$$

$$k_2 = \frac{\xi_y}{(\xi_x^2 + \xi_y^2)^{\frac{1}{2}}}$$

The eigenvalues for the above system are

$$\Lambda_A = \begin{bmatrix} U_c - K_\xi c & 0 & 0 & 0 \\ 0 & U_c & 0 & 0 \\ 0 & 0 & U_c + K_\xi c & 0 \\ 0 & 0 & 0 & U_c \end{bmatrix}$$

### Nonequilibrium

For nonequilibrium flow with two species the system has a rank of seven. Again, the equation was transformed to a general coordinate system then the eigenvalues and eigenvectors of the flux Jacobians were determined with Mathematica. The procedure, while involving significant analytical complexity, is straight forward. Extension for mixtures with additional species is also straight forward. These matrices are provided as follows:

$$\Lambda_A = \begin{bmatrix} U_c & 0 & 0 & 0 & 0 & 0 & 0 \\ 0 & U_c & 0 & 0 & 0 & 0 & 0 \\ 0 & 0 & U_c & 0 & 0 & 0 & 0 \\ 0 & 0 & 0 & U_c & 0 & 0 & 0 \\ 0 & 0 & 0 & 0 & U_c & 0 & 0 \\ 0 & 0 & 0 & 0 & 0 & U_c - K_f C & 0 \\ 0 & 0 & 0 & 0 & 0 & 0 & U_c + K_f C \end{bmatrix}$$

$$R_A = \begin{bmatrix} 0 & 0 & 0 & 1 & 0 & c_1 & c_1 \\ 0 & 0 & 0 & 0 & 1 & c_2 & c_2 \\ -k_2 & 0 & 0 & u & u & u-k_1c & u+k_1c \\ k_1 & 0 & 0 & v & v & v-k_2c & v+k_2c \\ (k_1v-k_2u) & 1 & 1 & \left(-\frac{X_1}{\kappa} + \frac{u^2+v^2}{2}\right) & \left(-\frac{X_2}{\kappa} + \frac{u^2+v^2}{2}\right) & (H-k_1uc-k_2vc) & (H+k_1uc+k_2vc) \\ 0 & 0 & 1 & 0 & 0 & e_1c_1 & e_1c_1 \\ 0 & 1 & 0 & 0 & 0 & e_2c_2 & e_2c_2 \end{bmatrix}$$

$$R_A^{-1} = \begin{bmatrix} k_2u-k_1v & k_2u-k_1v & -k_2 & k_1 & 0 & 0 & 0 \\ -e_2c_2b_1 & -e_2c_2b_2 & u(e_2c_2b_3) & v(e_2c_2b_3) & -e_2c_2b_3 & e_2c_2b_3 & 1+e_2c_2b_3 \\ -e_1c_1b_1 & -e_1c_1b_2 & u(e_1c_1b_3) & v(e_1c_1b_3) & -e_1c_1b_3 & 1+e_1c_1b_3 & e_1c_1b_3 \\ 1-e_1b_1 & -c_1b_2 & u(c_1b_3) & v(c_1b_3) & -c_1b_3 & c_1b_3 & c_1b_3 \\ -c_2b_1 & 1-c_2b_2 & u(c_2b_3) & v(c_2b_3) & -c_2b_3 & c_2b_3 & c_2b_3 \\ \left(\frac{b_1 + \frac{k_1u}{c} + \frac{k_2v}{c}}{2}\right) & \left(\frac{b_2 + \frac{k_1u}{c} + \frac{k_2v}{c}}{2}\right) & \left(\frac{-b_3u - \frac{k_1}{c}}{2}\right) & \left(\frac{-b_3v - \frac{k_2}{c}}{2}\right) & \frac{b_3}{2} & -\frac{b_3}{2} & -\frac{b_3}{2} \\ \left(\frac{b_1 - \frac{k_1u}{c} - \frac{k_2v}{c}}{2}\right) & \left(\frac{b_2 - \frac{k_1u}{c} - \frac{k_2v}{c}}{2}\right) & \left(\frac{-b_3u + \frac{k_1}{c}}{2}\right) & \left(\frac{-b_3v + \frac{k_2}{c}}{2}\right) & \frac{b_3}{2} & -\frac{b_3}{2} & -\frac{b_3}{2} \end{bmatrix}$$

where,

$$u_c = \xi_x u + \xi_y v \quad K_\xi = (\xi_x^2 + \xi_y^2)^{\frac{1}{2}}$$

$$b_3 = \frac{\kappa}{c^2} \quad b_2 = b_3 \left[ \left( \frac{u^2+v^2}{2} \right) + \frac{X_2}{\kappa} \right] \quad b_1 = b_3 \left[ \left( \frac{u^2+v^2}{2} \right) + \frac{X_2}{\kappa} \right]$$

$$k_1 = \frac{\xi_x}{(\xi_x^2 + \xi_y^2)^{\frac{1}{2}}} \quad k_2 = \frac{\xi_y}{(\xi_x^2 + \xi_y^2)^{\frac{1}{2}}}$$

The present study was concerned with only single species systems. Therefore, the first and second rows and columns of  $|\Lambda_A|$  are eliminated; the second and seventh rows and second and fifth columns in  $R_A$  are eliminated; the second and fifth rows and second and seventh columns of  $R_A^{-1}$  are eliminated. This reduces the rank of the system from seven to five.



## Bibliography

1. Anderson, J. A. Hypersonics and High Temperature Gas Dynamics. New York: McGraw-Hill Book Company, 1989.
2. Billig, F. S. "Shock-Wave Shapes Around Spherical- and Cylindrical-Nosed Bodies," Journal of Spacecraft and Rockets, Vol 4: 822-823 (June 1967).
3. Blackman, V. "Vibrational Relaxation in Oxygen and Nitrogen," Journal of Fluid Mechanics, Vol 1: pp. 61-85 (May 1956).
4. Candler, G. V. and McCormack R. W. "The Computation of Hypersonic Flows in Chemical and Thermal Nonequilibrium," Third National Aero-Space Plane Technology Symposium, Paper No. 017, June 1987.
5. Candler, G. and McCormack, R. "The Computation of Hypersonic Ionized Flows in Chemical and Thermal Nonequilibrium," AIAA Paper No. 88-0511, January 1988.
6. Chapman, S. and Cowling, T. G. The Mathematical Theory of Non-Uniform Gases. London: Cambridge Press, 1952.
7. Clarke, J. F. and McChesney, M. The Dynamics of Real Gas. London: Butterworth & Co., 1964.
8. Gaydon, A. G. and Hurle, I. R. The Shock Tube in High-Temperature Chemical Physics. New York: Reinhold Publishing Corporation, 1963.
9. Gnoffo, P.A., Gupta, R.N., and Shinn, J.L., "Conservation Equations and Physical Models for Hypersonic Air Flows in Thermal and Chemical Nonequilibrium," NASA Technical Paper 2867, February 1989.
10. Harten, A., Hyman, J.M. and Lax, P.D. "On Finite-Difference Approximations and Entropy Conditions for Shocks," Communications on Pure and Applied Mathematics, Vol 24: 297-322 (1976).
11. Harten, A. "Resolution Schemes for Hyperbolic Conservation Laws," Journal of Computational Physics, Vol 49: 357-393 (1983).
12. Hays, W. P. and Probstein, R. F. Hypersonic Flow Theory. New York: Academic Press, 1959.

13. Hertzberg, A. "The Application of the Shock Tube to the Study of the Problems of Hypersonic Flight," Jet Propulsion Journal of the American Rocket Society, Vol 26: 549-554 (July 1956).
14. Herzfeld, K. F. "The Rate and Mechanism of the Thermal Dissociation of Oxygen," 7th International Symposium on Combustion. London: Butterworth & Co., 1959.
15. Hirschfelder, J.O., Curtiss, C.F., Bird, R.B. Molecular Theory of Gases. New York: John Wiley & Sons Inc., 1964.
16. Hoffmann, K. A. (et al). "Effect of Dynamic Changes in Body Configuration on Shock Structure," AIAA Paper No. 89-0526, January 1989.
17. Kubota, T. "Investigation of Flow Around Simple Bodies in Hypersonic Flow," California Institute of Technology, Guggenheim Aeronautical Laboratory Hypersonic Wind Tunnel, Memorandum No. 40, June 1957.
18. Lambert, J. D. Vibrational and Rotational Relaxation in Gases. Oxford: Clarendon Press, 1977.
19. Landau, L. and Teller, E. "Zur Theorie der Schalldispersion," Physik A. Sowjetunion, B10: h.1, p34.
20. Lax, P.D. "Hyperbolic Systems of Conservation Laws and Mathematical Theory of Shock Waves," Siam Regional Series On Applied Mathematics, Vol 2 (1973).
21. Lees, L. "Laminar Heat Transfer Over Blunt-Nosed Bodies at Hypersonic Flight Speeds," Jet Propulsion Journal of the American Rocket Society, Vol 2: 259-269 (April 1956).
22. Lighthill, M. J. "Dynamics of a Dissociating Gas - Part I, Equilibrium Flow," Journal of Fluid Mechanics, Vol 2: 1-32 (January 1957).
23. Lighthill, M. J. "Dynamics of a Dissociating Gas - Part II, Quasi-equilibrium Transfer Theory," Journal of Fluid Mechanics, Vol 8: 161-182 (June 1960).
24. Liu, Y. and Vinokur, M. "Nonequilibrium Flow Computations I. An Analysis of Numerical Formulations of Conservation Laws," NASA Contractor Report 177489, Contract NAS2-11555, June 1988.
25. Liu, Y. and Vinokur, M. "Equilibrium Gas Flow Computations I. Accurate and Efficient Calculation of Equilibrium Gas Properties", AIAA Paper No. 89-1736, June 1989.

26. Lomax, H. and Inouye, M. "Numerical Analysis of Flow Properties About Blunt Bodies Moving at Supersonic Speeds in an Equilibrium Gas," NASA TR R-204, July 1964.
27. Matsuzaki, R. "Quasi-One-Dimensional Aerodynamics with Chemical, Vibrational and Thermal Nonequilibrium," Japan Society of Aeronautical Space Science, Vol 30, No 90: 243-258 (1987).
28. Millikan, R. C. and White, D. T. "Systematics of Vibrational Relaxation," Journal of Chemical Physics, Vol 39, No 12: 3209-3213 (December 1963).
29. Oliver, R. E. "An Experimental Investigation of Flow Over Simple Blunt Bodies at a Nominal Mach Number of 5.8," California Institute of Technology, Guggenheim Aeronautical Laboratory Hypersonic Wind Tunnel, Memorandum No. 26, June 1955.
30. Park, C. "Convergence of Computation of Chemical Reacting Flows," AIAA Paper No. 85-0247, January 1985.
31. Park, C. and Yoon, S. "A Fully-Coupled Implicit Method for Thermo-Chemical Nonequilibrium Air at Sub-Orbital Flight Speeds," AIAA Paper No. 89-1974, June 1989.
32. Park, C. "Assessment of Two-Temperature Kinetic Model for Ionizing Air," Journal of Thermophysics, Vol 3, No 3: 233-244 (July 1989).
33. Prabhu, D. K. and Tannehill, J. C. "Numerical Solution of Space Shuttle Orbiter Flow Field Including Real Gas Effects," AIAA Paper No. 84-1747, June 1984.
34. Pulliam, T. H. and Steger J. L. "Recent Improvements in Efficiency, Accuracy, and Convergence for Implicit Approximate Factorization Algorithms," AIAA Paper No. 85-0360, January 1985.
35. Roe, P. L. "Approximate Riemann solvers, Parameter Vectors, and Difference Schemes," Journal of Computational Physics, Vol 43: 357-372 (1981).
36. Roe, P. L. "Characteristic-Based Schemes for the Euler Equations," Annual Review of Fluid Mechanics, Vol 18: 337-365 (1986).
37. Scherr, S. and Shang, J. "Flows Over Blunt Bodies Using a Flux-Splitting and Shock-Fitting Scheme," AIAA Paper No. 86-0340, January 1986.

38. Shang, J. S. "Numerical Simulation of Wing-Fuselage Aerodynamic Interaction," AIAA Journal, Vol 22, No 10: 1345-1353, October 1984.
39. Shang, J. S. and Josyula, E. "Numerical Simulations of Nonequilibrium Hypersonic Flow Past Blunt Bodies," AIAA Paper No. 88-0512, January 1988.
40. Stalker, R. J. "Hypervelocity Aerodynamics with Chemical Nonequilibrium," Annual Review of Fluid Mechanics, Vol 21: 37-60 (1989).
41. Vincenti, W. G., and Kruger, C. H. Jr Introduction to Physical Gas Dynamics. New York: John Wiley and Sons, Inc., 1986.
42. Vinokur, M. and Liu, Y. "Equilibrium Gas Flow Computations II. An Analysis of Numerical Formulations of Conservation Laws," AIAA paper No. 88-0127, January 1988.
43. Wada Y., Ogawa S., Ishiguro T., Kubota H., "A Generalized Roe's Approximate Reimann Solver for Chemically Reacting Flows," AIAA Paper No. 89-0202, January 1989.
44. Wang, J. C. T. and Widhopf, G. F. "A High-Resolution TVD Finite Volume Scheme for the Euler Equations in Conservation Form," AIAA Paper No. 87-0538, January 1987.
45. Yang, J. Y. "Numerical Solution of the Two-Dimensional Euler Equations by Second-Order Upwind Difference Schemes," AIAA Paper No. 85-0292, January 1985.
46. Yee, H.C. and Kutler, P., "Application of Second-Order-Accurate Total Variation Diminishing (TVD) Schemes to the Euler Equations in General Geometries," NASA TM-85845, August 1983.
47. Yee, H.C., "A Class of High-Resolution Explicit and Implicit Shock-Capturing Methods," NASA TM-101088, February 1989.

### Vita

Ken Moran [REDACTED] He attended high school at Robinson High School and graduated in June of 1980. He then went on to attend Virginia Tech where he obtained his Bachelor of Science degree in Aerospace Engineering in December of 1984. He received his commission into the United State Air Force through the ROTC program. His initial assignment was at the 49th Test Squadron at Barksdale AFB, LA where he flew as a flight test engineer. In 1986 he was recognized as an "Outstanding Young Man of America." After four years in weapons testing, he attended and completed Squadron Officer School in October 1988, where he was recognized as a distinguished graduated. Following this he attended the Air Force Institute of Technology, at Wright-Patterson AFB, to complete a Master of Science degree in Aeronautical Engineering.

[REDACTED]

December 1990      Master's Thesis

A COMPARISON OF MOLECULAR VIBRATION MODELING  
FOR THERMAL NONEQUILIBRIUM AIRFLOW

Kenneth J. Moran, Capt, USAF

Air Force Institute of Technology  
WPAFB OH 45433-6583

AFIT/GAE/ENY/90D-17

Dr. Joseph S. Shang  
WRDC/FIMM  
Wright-Patterson AFB, OH  
45433

Approved for public release; distribution  
unlimited

The effects of thermal nonequilibrium on flows about blunt-bodies have not been studied numerically in isolation from chemical reactions. Typically, air is modeled as a perfect gas or as a chemically reacting mixture. In the former case, significant errors result at Mach numbers exceeding about 5. However, below Mach numbers around 8, the effects of chemical reactions are negligible. This study analyzes flow about a simple axisymmetric blunt-body at moderate hypersonic speeds (Mach numbers between 5-8). A first-order-accurate Roe scheme was used to compute solutions of the Euler equations assuming different gas models: perfect gas, thermal equilibrium, and thermal nonequilibrium. Equilibrium and nonequilibrium shock standoff distances deviated 10-15 percent from perfect gas calculations. Nonequilibrium solutions produced striking temperature and density gradients in the stagnation region with a unique "hot spot" near the shock.

Axisymmetric Flow, Thermal Nonequilibrium, TVD Scheme, 99  
High-Temperature, Molecular Vibration, Equilibrium, 702

Unclassified

Unclassified

Unclassified

UL